

https://dspace.org/

Cross-section transmission electron microscopy of radiation damage in diamond

Nshingabigwi, Emmanuel Korawinga

2008-03-06T07:29:49Z
http://hdl.handle.net/10539/4539

Downloaded from a DSpace repository. https://dspace.org/

CROSS-SECTION TRANSMISSION ELECTRON MICROSCOPY OF RADIATION DAMAGE IN DIAMOND

By

Emmanuel Korawinga Nshingabigwi

A dissertation submitted to the Faculty of Science, University of the Witwatersrand, Johannesburg, in fulfilment of the requirements for the degree of Master of Science.

Johannesburg, 2006.

Declaration

I declare that this dissertation is my own unaided work. It is being submitted for the degree of Master of Science in the University of the Witwatersrand, Johannesburg. It has not been submitted before for any degree or examination in any other university.

_____

(Signature of candidate)

_____day of_____2006

Abstract

Diamond is nowadays regarded as a potential semiconductor material of the future, due to its extreme and unique properties. Some of these properties, include its high hardness, highest breakdown field, high Debye temperature, high thermal conductivity, high hole and electron mobilities, large bandgap and optical transparency, among others. These properties make diamond suitable for high-temperature, high-speed and high-power electronic applicatons, as well as in other applications. However, defects associated with ion implantation have been shown to make it rather difficult to obtain n-type doping in diamond. As such, an understanding of the nature of defects produced during ion implantation of diamond remains a subject of great importance, if not essential, for the optimization of high-temperature, high-power electronic applications in particular. In this respect, this study investigates the nature of the radiation damage generated within the collision cascades of multi-implantations of carbon ions in high-pressure, high-temperature single-crystal synthetic type Ib diamond, spread over a range of energies (50-150keV) and doses. This is achieved by means of the cold-implantation-rapid-annealing (CIRA) routine, and the analysis of damage caused was done by using cross sectional transmission electron microscopy techniques. More precisely, the modes used to achieve this are the bright field transmission electron microscopy (BFTEM) coupled with selected area diffraction or SAD.

At low dose implantation or at sub-critical implantation doses (2.5×10^{15} ions/cm^2), it was found that the ion-damaged diamond layer consists of some threading dislocations, not homogeneously distributed which propagate from the surface into the ion-damaged diamond.

In contrast to the sub-critical implantation doses , it was found that at very high implantation doses (7.0×10^{15} ions/cm^2), i.e., above the critical dose (where

diamond transforms to graphite upon annealing), the damaged diamond layer had some unconventional defect features close to the implanted surface.

To my family.

Acknowledgements

I would like to express my heartfelt gratitude and appreciation to both my supervisors Profs. T.E. Derry and Jan Neethling. It was through their concerted efforts, brainstorming and guidance that this dissertation became a success.

I am also indebted to De Beers Industrial Diamond Division (Pty) for providing all the diamond samples used in this study. The technical assistance and devotion of Mik Rebak, especially during the lengthy mechanical polishing of the samples down to sub-50μm and for the design of the diamond holder is gratefully acknowledged.

I would like to thank also Dr. Charles Levitt for his availability while preparing the annealing setup for the Rapid Thermal Annealing (RTA) technique. Special mention must be made of S.R. Naidoo-for his assistance in conducting the implantations for all my samples and N.W. Makau and all my fellow students for the many fruitful discussions that we had . I would like to express also my gratitude to Benjamin Emmerick Jeremy for his invaluable help while laser-cutting all my cross-sectional electron microscope (TEM) specimens.

I am grateful to the University of the Witwatersrand, the School of Physics, particularly, the DST/NRF- Centre of excellence in Strong Materials, iTHEMBA LABS-Gauteng for their financial support. The ion milling and the transmission electron microscopy (TEM) investigations were carried out by Prof. JH Neethling at the Nelson Mandela Metropolitan University. His expertise is highly acknowledged.

Finally, may those who helped me directly or indirectly and whose names are not mentioned, find here my sincere gratitude.

Emmanuel K Nshingabigwi
Johannesburg
2006

Contents

Declaration i

Abstract ii

Acknowledgements iii

List of Figures vi

List of Tables ix

1 Introduction 1
- 1.1 Motivation . . . 1
- 1.2 Dissertation Breakdown . . . 4

2 Theoretical Background 5
- 2.1 Layout of the Chapter . . . 5
- 2.2 Diamond and Graphite . . . 5
  - 2.2.1 Crystallographic Structures . . . 5
  - 2.2.2 Properties of Diamond and Graphite . . . 9
  - 2.2.3 Phase Diagram of Carbon . . . 12
  - 2.2.4 Classification of Diamond . . . 14
  - 2.2.5 High-pressure High-temperature (HPHT) Diamond Synthesis . . . 17
  - 2.2.6 Some applications of Diamond . . . 20
  - 2.2.7 The doping of Diamond . . . 21
- 2.3 Energy-loss mechanisms . . . 22
- 2.4 Radiation Damage . . . 29
  - 2.4.1 Point defects . . . 31
  - 2.4.2 Line defects . . . 33
  - 2.4.3 Planar defects . . . 37
  - 2.4.4 Other defects . . . 39

3 Experimental Techniques 40
- 3.1 Layout of the Chapter . . . 40
- 3.2 Equipment used . . . 40

3.2.1 The Ion Implanter 40
3.2.2 The Ion Mill 44
3.2.3 The Transmission electron Microscope 46
3.3 The specimen preparation 55
3.3.1 Mechanical Polishing 56
3.3.2 Implanting 58
3.3.3 Annealing 61
3.3.4 Ion Milling 63

4 Results **66**
4.1 Layout of the Chapter 66
4.2 TRIM simulation of ion implantation 66
4.3 Bright field transmission electron microscopy and diffraction . . 68
4.3.1 TEM results of the low dose carbon implanted diamond sample 68
4.3.2 TEM results of the high dose carbon implanted diamond sample 71

5 Discussion and Conclusions. **73**
5.1 Discussions 73
5.2 Conclusion 75

References **76**

List of Figures

2.1 Face-centred cubic structure of diamond. (After ref [14]). 6

2.2 The diamond structure seen along various directions. (After ref [15]) The panel on the bottom left hand side shows the [111] direction, while the top right hand side shows the [110] direction . 6

2.3 Crystal structure for graphite showing ABAB stacking sequence and unit cell. (After ref [17]). 8

2.4 Energy level diagram for the transformation between graphite and diamond. (After ref [23]). 10

2.5 P,T phase diagram of carbon. (After ref [21]). 12

2.6 Classification scheme for diamond. (After ref [35]). 16

2.7 The diagram of the capsule for growing large diamonds. There is usually a temperature difference of about 30°C between the centre of the capsule and the seed pad (After ref [40]). 18

2.8 Dependence of the nuclear and electronic energy loss (stopping power) on the energy of the projectile, in the case of the implantation of carbon ions into diamond (After ref [7]). 25

2.9 Gaussian distribution of implanted ions (After ref [57]). 27

2.10 Example of typical defects by ion implantation (After ref [7]). . 30

2.11 Different types of point defects in diamond (After ref [15]). . . . 31

2.12 Structure of the <110>-split interstitial, showing the two atoms (in red) forming the interstitial pair, and their neighbours (in blue) (After ref [63]). 32

2.13 Edge and Screw dislocation in a simple cubic lattice (After ref [65]) The panel on the left hand side shows an edge dislocation while the right side one shows a screw dislocation. In these diagrams, l is the line direction, b is the Burgers vector defined by the closure fault of the Burger circuit (in red). 33
2.14 Dislocation glide in a simple cubic lattice (After ref [65]). 35
2.15 Dislocation climb in a simple cubic lattice (After ref [65]). . . . 36
2.16 Small angle grain boundary (After ref [67]). 37
2.17 The arrangement of the atoms on either side of a twin interface (After ref [72]). 38

3.1 A schematic diagram of the model 200-20AF Ion Implanter. (After ref [74]). 41
3.2 A schematic illustration of the PIPS work chamber showing the Penning Ion gun, the specimen exchange mechanism, the Faraday cup, the airlock and the specimen post. (After ref [76]). 45
3.3 Interaction between electrons and material. (After ref [77]). . . . 46
3.4 Schematic illustration of a transmission electron microscope. (After ref [78]) The panel on the left hand side shows a simplified representation of the TEM setup, while the right hand side one shows the two basic imaging modes. 50
3.5 Bragg diffraction in the TEM sample (After ref [65]). g denotes the corresponding diffraction vector. 51
3.6 Microdiffraction mode. (After ref [77]). 51
3.7 Schematic of a spectrometer system for recording energy-loss spectra and energy filtered images. Electron paths are arrowed. (After ref [80]). 53
3.8 A simplified energy-loss spectrum. (After ref [80]) (a) Low-loss spectrum and (b) The core-loss region (recorded with higher detector sensitivity) showing several basic shapes of ionization edge, each superimposed on a spectral background (dashed curves). . 54
3.9 Enlarged schematic view of the diamond implant situation, to scale. 55
3.10 A photograph of thin diamond holder. 59

3.11 Horizontal Split Tube Furnace (STF). (After ref [91]). 61
3.12 Schematic diagram of the quartz worktube. Some argon flows continuously out of the entry funnel, preventing the ingress of air. 62
3.13 Photograph of a pair of thin slice diamond samples. 63
3.14 Schematic diagram of principle of preparation and mounting of diamond samples for ion beam damage studies by X-TEM. . . . 64
3.15 Scanning electron microscope (SEM) images of the cross-sectional ion milled diamond TEM sample. TEM investigation were carried out at the edge of the hole at the diamond/diamond interface 65

4.1 A TRIM-92 simulation of the damage (vacancy) distribution produced by the carbon ion multi-implantation. (After ref [10]). . . 67
4.2 Cross-sectional bright-field TEM micrographs and diffraction pattern of the low dose ion-implanted diamond surface . The arrows in (a) and (b) indicate the direction of ion implantation and the point of the arrow shows the diamond/glue interface. The diffraction pattern in (c) indicates that (a) and (b) were recorded with a <110> beam direction and 220 type reflection 70
4.3 Cross-sectional bright-field TEM micrographs and diffraction pattern of an unimplanted diamond surface . The arrow in (a) indicates the diamond/glue interface. The diffraction pattern in (b) indicates that (a) was recorded with a <110> beam direction and 220 type reflection 71
4.4 Cross-sectional bright-field TEM micrographs and diffraction pattern of the high dose implanted diamond surface . The arrows in (a) to (d) indicate the direction of the ion implantation and the point of the arrow shows the diamond/glue interface. The diffraction pattern in (e) were recorded with a <110> beam direction and 111 type reflection. The magnification of the microcraphs in (a) to (d) are indicated in (a). 72

List of Tables

2.1 Some of the properties of graphite and diamond 11
2.2 The ranking of various catalysts that are used in the growth of diamond. (After ref [15]). 17

3.1 Implantations parameters. (After ref [10]) 59

Chapter 1

Introduction

1.1 Motivation

Diamond is regarded nowadays as a potential semiconductor of the future, due to its extreme and unique properties. Some of these properties, include its high hardness, highest breakdown field, high Debye temperature, high thermal conductivity, high hole and electron mobilities, large bandgap and optical transparency among others. These extreme and unique properties make diamond suitable for high-temperature, high-speed and high-power electronic applicatons, as well as in other applications.

As far as diamond electronic applications are concerned, ion implantation has been shown to be the preferred method for its doping because it offers both spatial and depth control not achievable using diffusion or growth methods [1]. However, ion implantation is a harsh, non-equilibrium method used to insert atoms into a material [2], and it often introduces radiation damage in the crystalline structure of diamond. The radiation effects due to ion implantation have been shown by previous studies to be deleterious to the performance of some materials [3].

In spite of this, radiation damage has also been shown to have useful effects on materials. In particular, it is known that it can be repaired, if the annealing temperature and the damage level are kept below a critical value [4] but most importantly, Vickerman [5] stresses that without damaging a surface, one can not get any information from it.

In addition, defects associated with ion implantation have been shown to be responsible for trapping in doped diamond and may be responsible for the difficulty in obtaining n-type doping in diamond [4].

As such, an understanding of the nature of defects produced during ion implantation of diamond remains a subject of great importance if not essential for the optimization of high-temperature, high-power electronic applications.

Radiation damage in diamond for semiconducting applications has been studied extensively over the last thirty years [2] and yet, as reported by Derry et al. [6], unsolved problems including the origin and the nature of the deep and ultra deep damage observed in certain cases, still remain.

Dresselhaus et al. [7] recommended in the early nineties, the use of cross-sectional transmission electron microscopy (XTEM) as an effective method of revealing vacancy-rich and interstitial rich regions in the implantation-affected volume but to our knowledge, this hasn't been attempted yet. Also, Orwa et al. [8] emphasized that while the macroscopic changes which occur in ion irradiated diamond are known, the microscopic nature of the damage is not clear, partially due to the absence of detailed transmission electron microscopy (TEM) studies of ion-irradiated diamond.

It is important to mention that, although a lot of work involving radiation-induced effects in diamond using various characterization techniques has been carried out thus far, one can say that cross-section transmission electron microscopy hasn't been exploited fully, partly due to the difficulties associated with the cross-sectional TEM specimen preparation [7, 9] which requires great

skills, stamina and a lot of patience.

The ion doses (low or high) at which ion implantation in diamond is performed may lead to different kinds of damage which need further investigation. Indeed, Spits et al. [10] highlighted that, owing to the fact that diamond is a metastable form of carbon, there is a limit placed upon how much damage an implanted layer can suffer before irreversible structural changes occur, which in the extreme case (corresponding to very large implantation), may lead to graphitization of the implanted layer. The critical dose at which this process occurs is approximately $5.2\text{x}10^{15}$ ions/cm^2 [10].

Kalish et al. [11] have studied the nature of damage in ion-implanted and annealed diamond using Raman Spectroscopy. They reported that for low dose implantations (which create damage below the critical dose), the diamond is rich in point defects and anneals easily back to diamond, via some well-defined defect states (most likely the split interstitial dumbbell). They also found that, implantation to doses which creates damage in excess of the critical dose, results in a fully amorphised, mostly sp^2 bonded, material which converts to graphite upon annealing.

This study investigates the nature of the radiation damage generated within the collision cascades of multi-implantations of carbon ions in diamond spread over a range of energies and doses by means of cold-implantation-rapid-annealing (CIRA) routine using cross sectional transmission electron microscopy techniques.

1.2 Dissertation Breakdown

The first chapter presents the motivation and the outline of this dissertation. Chapter 2 gives an overview of the theoretical background of this study. In this chapter, attention is given particularly to theories related to energy-loss mechanisms and radiation damage in diamond. Chapter 3 outlines the experimental techniques i.e. the equipment used and the specimen preparation techniques are briefly discussed. Chapter 4 is dedicated to the results obtained from the radiation damage in diamond while Chapter 5 is devoted to in-depth discussion and conclusions.

Chapter 2

Theoretical Background

2.1 Layout of the Chapter

This chapter gives an overview of the theoretical background of this study. The first section discusses some properties and characteristics of the two main allotropes of carbon, which are diamond and graphite, with much emphasis on diamond. The second section discusses the slowing down processes of ions into diamond while the last section outlines the radiation damage in diamond, stressing the most expected type in this study, namely, the line defects.

2.2 Diamond and Graphite

2.2.1 Crystallographic Structures

In pure natural diamond, carbon atoms are bound to four adjacent atoms placed at the corners of a regular tetrahedron forming single σ bonds (0.154 nm), which result in sp^3- hybridized orbitals in the direction of the cube diagonals and the bonds form equal angles of 109.4° to each other [12]. The diamond structure can be viewed as two interpenetrating face-centred cubic structures displaced by $(\frac{1}{4}, \frac{1}{4}, \frac{1}{4})a$ along the body diagonal as shown in figure 2.1, where a is the edge length of the cubic unit cell and has a value of 3.567 Å [13].

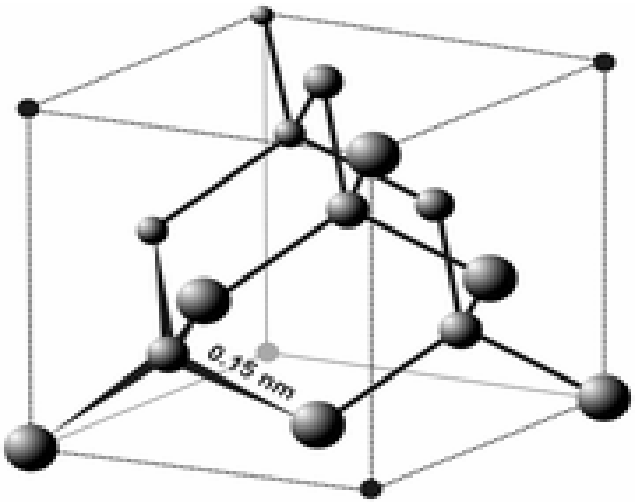


Figure 2.1: Face-centred cubic structure of diamond. (After ref [14]).

The different structures of diamond viewed from various directions are shown in figure 2.2.

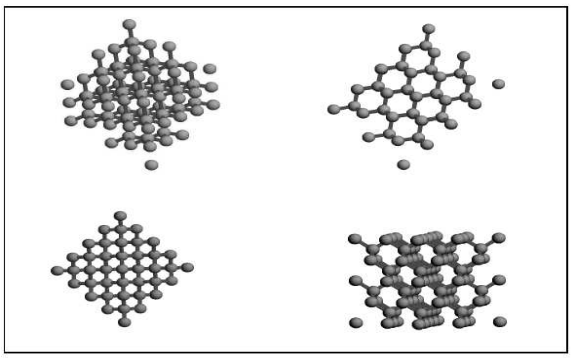


Figure 2.2: The diamond structure seen along various directions. (After ref [15]) The panel on the bottom left hand side shows the [111] direction, while the top right hand side shows the [110] direction .

Notice that the [110] direction (top right) offers wider channels than the [111] direction (bottom left). The nearest-neighbour carbon-carbon distance is 1.544Å, nearly 10% larger than in graphite, yet the density of diamond ($1.77\text{x}10^{23}\text{cm}^{-3}$) is 56% higher than in graphite, due to the higher anisotropy of the graphite structure [7].

The diamond crystal, in contrast to graphite, is highly symmetric with a cubic space group Fd3m - $O^7{}_h$ [7]. Furthermore, diamond and graphite cleave along {111} and {001} planes respectively [16]. There also exists a rare hexagonal form of diamond with space group $D^4{}_{6h}$ or P 6_3 / mmc, the same as for graphite, but with different site locations [7].

Graphite is composed of a series of stacked parallel planes shown schematically in figure 2.3.

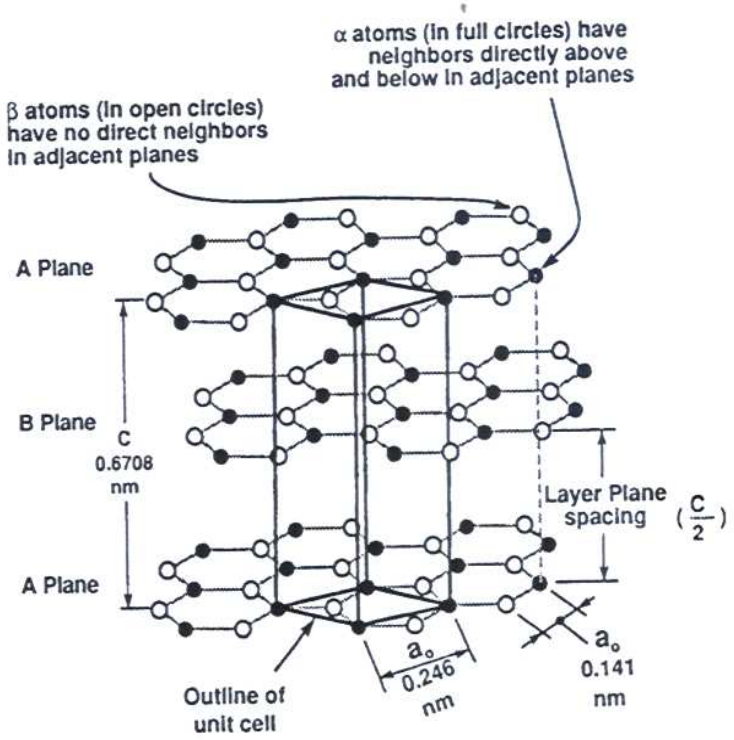


Figure 2.3: Crystal structure for graphite showing ABAB stacking sequence and unit cell. (After ref [17]).

These (parallel planes) have the ABAB planar stacking arrangement as shown in figure 2.3, and they have an in-plane nearest-neighbour distance of 0.141nm, a c-axis lattice constant of 0.6708 nm, and an interplanar distance of 0.335 nm [7, 17]). In addition, the graphite crystal is described by the D^4_{6h} or P 6_3 / mmc space group and has four atoms per unit cell [7].

2.2.2 Properties of Diamond and Graphite

Diamond is the metastable form of carbon, which converts to graphite under annealing [18] while graphite is the thermodynamically stable form of carbon at room temperature and pressure [19]. In addition, diamond is the hardest (least deformable) material known at the moment with a value approximately double that of cBN, which, in turn is twice as hard as the conventional abrasives [12]. Graphite is the stiffest material in nature meaning that it has the highest in-plane elastic modulus [7]. Also, graphite is opaque while diamond is transparent over a wide range of wavelengths [20].

Diamond is an indirect gap semiconductor, with a bandgap value of 5.48 eV at 77K and 5.47 eV at 300K [18] while graphite can be, electrically, considered as a semi-metal, that is a conductor in the basal (ab) plane and an insulator along the c-axis [17] . Diamond is also completely resistant to all chemical etchants at room temperature while graphite can be etched by some very active boiling mixtures of acids (for example, 1:1:1 of HNO_3; H_2SO_4; $HClO_4$) and therefore, this difference between graphite and diamond surfaces can be exploited to remove graphite from diamond [7]. Both diamond and graphite have two principal crystallographic forms: 'hexagonal' and rhombohedral graphite; and 'hexagonal' and 'cubic' diamond. The slight crystallographic differences are the result of different sequences of layering in the crystal [21]. In each of the hexagonal types of graphite and diamond the layering sequence is ABABAB - ; that is the third layer of atoms exactly superposes the first layer while in 'rhombohedral' graphite and 'cubic' diamond the layering sequence is ABCABC - ; that is the fourth layer exactly superposes the first layer [21]. Graphite consists of carbon atoms bonded into hexagonal sheets (sp^2-type bonding) with only weak forces between the sheets, while by contrast, diamond displays fourfold sp^3-type bonding [20]. Diamond and graphite have similar standard enthalpies

(the difference between them is only 2.9 kJmol^{-1}), but the activation barrier between them is very large as shown in figure 2.4, giving the energy level diagram for the transformation between graphite and diamond [22].

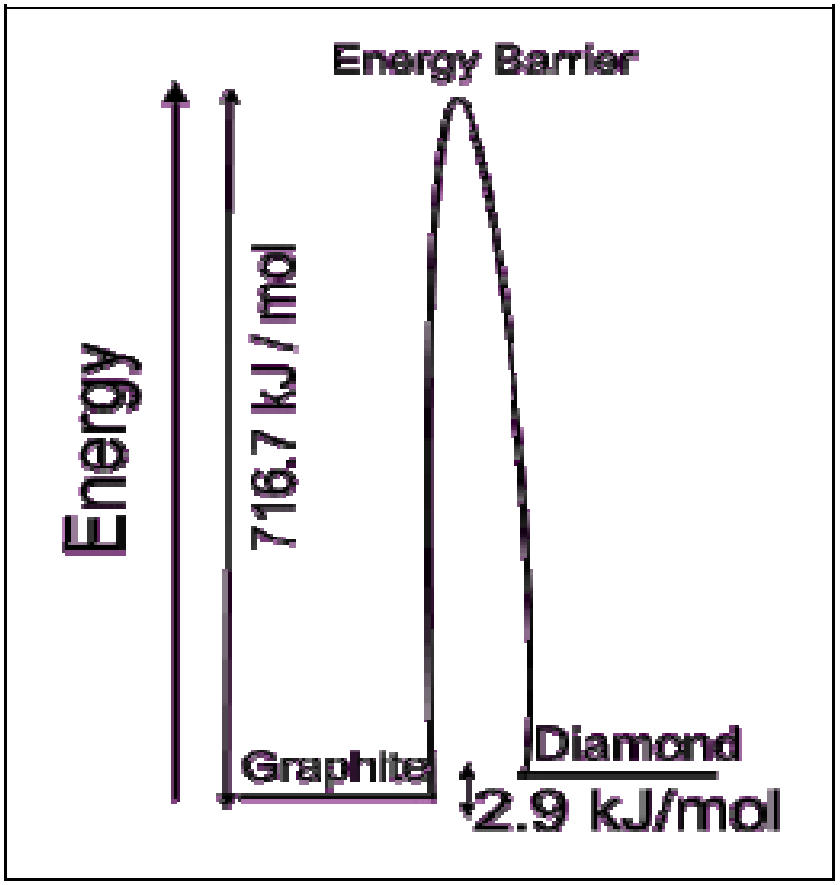


Figure 2.4: Energy level diagram for the transformation between graphite and diamond. (After ref [23]).

Some of the properties of graphite and diamond are shown in Table 2.1.

Table 2.1: Some of the properties of graphite and diamond

	Graphite[a]	Diamond
Lattice Structure	Hexagonal	Cubic
Space group	D^4_{6h} or P 6_3 / mmc	Fd3m - O^7_h
Cell constant at 298K [nm]	0.2462[c]/0.6708[c]	0.3567[b]
Density at 298K [g/cm^3]	2.26[c]	3.515[c]
Carbon-carbon bond distance [nm]	0.141[b]	0.15445[b]
Effective Debye temperature at (293-1100)[K]	2500[c]/950[c]	1860±10[b]
Thermal conductivity at RT,Type IIa [W/m.K]	398[b]/2.2[b]	2000-2100[b]
Linear thermal expansion at RT [/K]	-1x10^{-16}[c]/+27x10^6	0.8x10^{-6}[b]
Index of refraction at 546.1nm [nm]	- / -	2.4237[b]
Resistivity (Type I and most Type IIa [Ω.m])	2.5-5.0x10^{-6}/3x10^{-3}[b]	10^{18}[b]
Dielectric constant at 300K	3.0[c]/5.0[c]	5.70±0.05[b]
Specific heat,C_p at 300K [J/mol.K]	8.033-8.635[b]	6.125[b]
Electron mobility[cm^2/V.s]	20000[c]/100[c]	2200[b]
Hole mobility[cm^2/V.s]	15000[c]/90[c]	1600[b]
Atomic density[cm^{-3}]	1.14x10^{23}[c]	1.77x10^{23}[c]
Band gap[eV]	-0.04[c]	5.47[c]
Melting point[K]	4200[c]	4500[c]
Raman frequency[cm^{-1}]	1582[c]	1332[c]
Hardness[GPa]	- / -	98
Velocity of sound[cm/s]	2.63x10^5[c]/∼1×10^5	∼1.96x10^5[c]
Ionization energy of B Acceptor[eV]	- / -	0.37[d]
Ionization energy of N as Donor[eV]	- / -	1.7[d]
Ionization energy of P as Donor[eV]	- / -	0.59[d]
Breakdown field[V/cm]	- / -	10^7[c](highest)

[a]Anisotropic quantities are given first as the basal plane value, then the normal to the basal plane value.

[b][17],[c][7],[d][24].

2.2.3 Phase Diagram of Carbon

Figure 2.5 shows a phase diagram for carbon, where, the solid lines represent the equilibrium phases boundaries. Three major lines are worthy mentioning here. These include:

• The boundary between the graphite and the diamond stable regions which runs from 1.7 GPa/0K, to the graphite/diamond/liquid triple point at about 12 GPa/5000K, and this is the so-called Berman-Simon line (B-S line) [21, 25].

• The melting line of graphite extending from the graphite/ liquid/vapor triple point at 0.011GPa/5000K to the graphite/ diamond/liquid triple point [21].

• The diamond melting line that runs to high pressures and temperatures above the triple point [21].

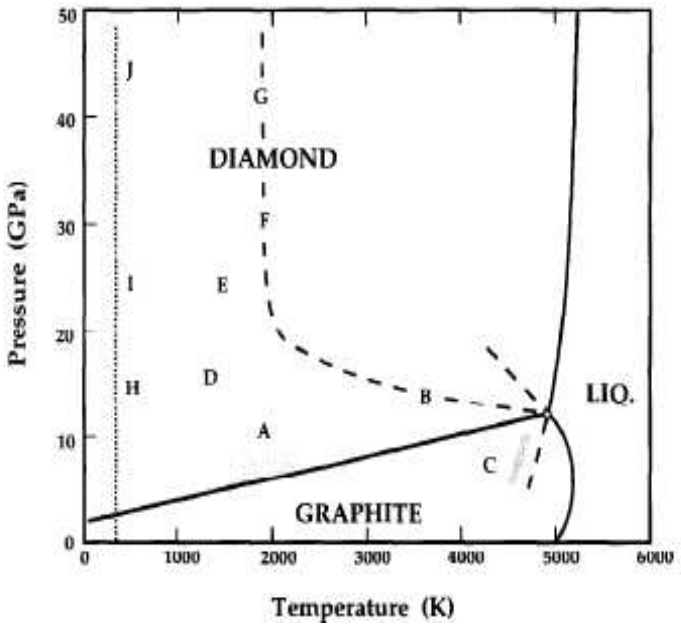


Figure 2.5: P,T phase diagram of carbon. (After ref [21]).
. Letters A,B,C,D,E,F and G show different regions within the phase diagram.

The following deductions can be made from figure 2.5, as alluded to by Bundy FP et al [21]:

• The commercial synthesis of diamond from graphite by catalysis is feasible in the region A.

• Region B is the P/T threshold of very fast (less than 1ms) solid-solid transformation of graphite to diamond.

•Region C is the P/T threshold of very fast transformation of diamond to graphite.

• Region D is the region where single crystal hexagonal graphite transforms to retrievable hexagonal-type diamond.

• Region E marks the upper ends of shock compression/ quench cycles that convert hex-type graphite particles to hex-type diamond.

• Region F designates the upper ends of shock compression/ quench cycles that convert hex-type graphite to cubic-type diamond.

• Region B-F-G indicates the threshold of fast P/T cycles that convert either type of graphite or hexagonal diamond into cubic-type diamond.

• Region H-I-J denotes the path along which a single crystal hex-type graphite compressed in the c-direction at room temperature loses some graphite characteristics and acquires properties consistent with diamond-like polytype, but reverses to graphite upon release of pressure.

2.2.4 Classification of Diamond

Diamonds are categorized according to the form and the amount of the dominant defects (nitrogen-N) that they contain. The N-containing diamonds are called type I and the N-free (essentially) type II stones [15].

Type I diamonds are subclassified into type Ia and type Ib depending on the aggregation of N atoms in the lattice [13]. Type Ia, which contains nitrogen in non-paramagnetic aggregated form, is the most abundant type in nature [26].

Type IaA have N (nitrogen) in what is called the A-aggregate form, viz., in substitutional pairs [27]. Diamonds called type IaB have the nitrogen in a highly symmetric form of 4N atoms surrounding a vacancy [28]. Also, nitrogen-containing platelets (B'-defects) are known as IaB' [29]; type IaB' regular, belongs to diamonds with a quite high content of B'-defects; type IaB' irregular,has got a low content of B'-aggregates, while, type IaB without B' defects comprises type IaB diamonds not containing platelets [30, 31, 32].

Type Ib stones [18] contain nitrogen mostly in single substitutional, paramagnetic form and they are very rare ($\sim 0.1\%$) in nature, but most high-pressure, high-temperature (HPHT) and many chemical vapor deposition (CVD) diamond are mainly of this type. The appearance of type Ib diamond is usually a deep golden-yellow which tends to be greenish when containing a high density of substitutional nitrogen [26].

The substitutional N forms a deep donor (E_a = 1.7 eV) [12], making it unsuitable for electronic applications. However the properties of type Ib stones [26] may be used as standard tests when attempting to dope a pure diamond substrate with nitrogen-ion implantation. Note in passing that some authors [29] categorize type Ic as diamonds with high concentration of dislocations but this labelling is not based on the presence of nitrogen.

Type II stones are subclassified in types IIa and IIb and are nitrogen-poor.

Type IIa diamonds are the purest form of diamond [12]. They are also rare, optically the most transparent of all diamonds [33] and exhibit the intrinsic semiconducting properties of diamond with a wide bandgap of 5.47 eV.

Type IIb diamond has a relatively high boron (B) concentration compared to nitrogen and the uncompensated boron makes it a p-type semiconductor [34]. In nature, these diamonds, which are very rarely found, have a maximum boron concentration of 10^{17} cm^{-3} and on the other hand, the man-made equivalents, by HPHT as well as CVD techniques, can contain as much as $10^{20}cm^{-3}$ [33]. Because of the presence of boron, type IIb diamonds are coloured blue. In spite of these definite classifications, Antonella [12] amongst others, warns that one must bear in mind that many crystals are rather inhomogeneous and a mixture of different types may be present in the same diamond sample.

Figure 2.6 summarizes the diamond classification.

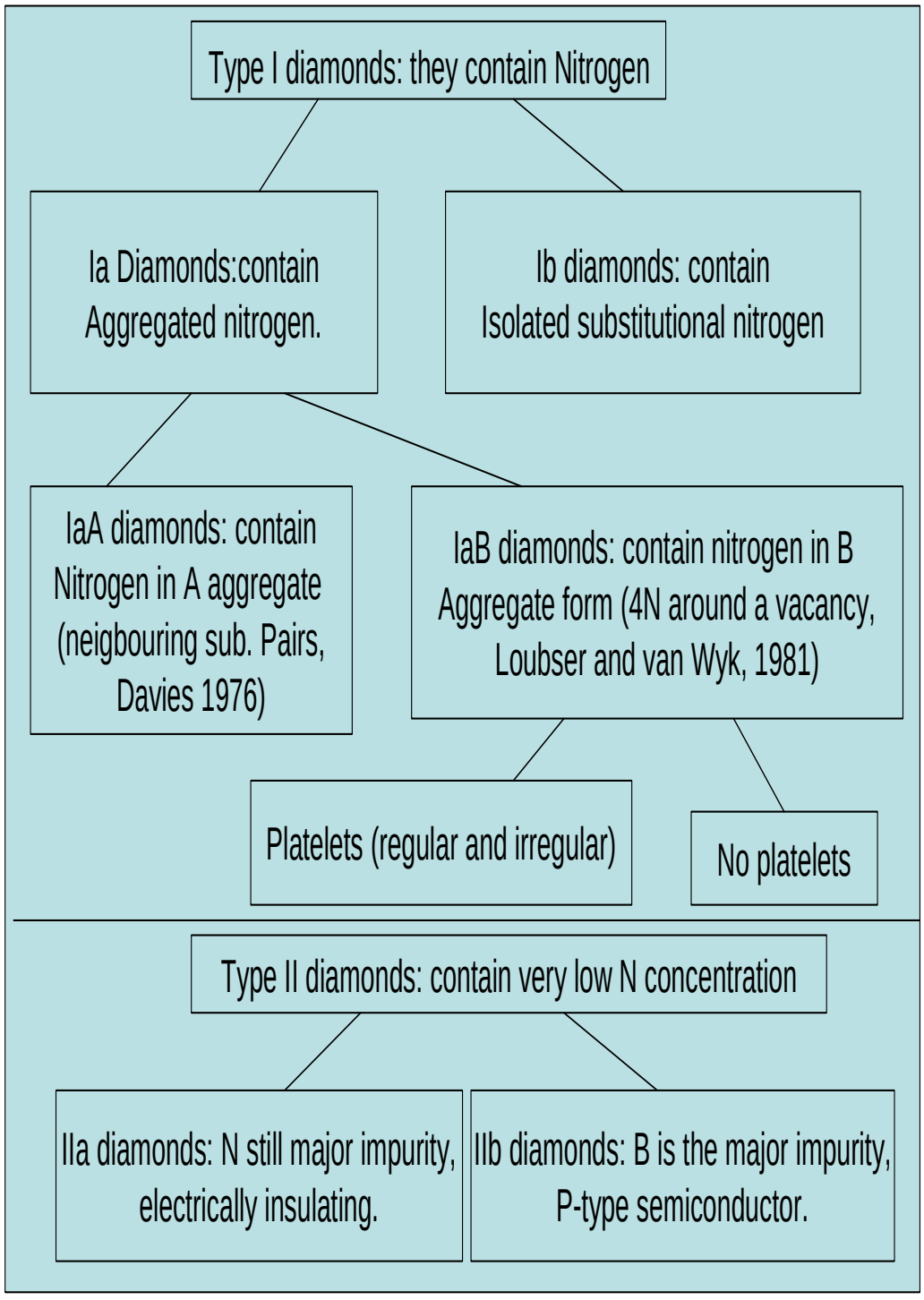


Figure 2.6: Classification scheme for diamond. (After ref [35]).

2.2.5 High-pressure High-temperature (HPHT) Diamond Synthesis

The existence of a large activation barrier between graphite and diamond phases as seen in Figure 2.4 prevents interconversion between them, at room temperature and atmospheric pressure. Hence, the only way to synthesize diamond from graphite is to use a high pressure high temperature (HPHT) method, based on the imitation of the natural circumstances under which natural diamond is formed [33]. However, in the beginning, it was shown that the transformation of graphite to diamond decreases with increasing pressure; making this process slow and inefficient for useful applications [36, 37]. Fortunately, it was realized that some form of catalyst/solvent was important to dissolving the graphite and it was found that by using such a catalyst/solvent, diamond could already be synthesized between 5 GPa and 10 GPa, in the temperature range 1300°C -2300°C [15, 34]. The rôle of the metal-solvents is to dissolve carbon extensively and to transport the carbon to the growing diamond surface. Thus, the catalysts help in the formation of a supersaturated carbon solution [38]. Then, this catalyst solution is held at the temperature and pressure conditions under which diamond grows, allowing a faster conversion under easier and cheaper conditions [39].

The 'top five'catalysts are shown in Table 2.2, cobalt being judged to be the best of the catalysts for the formation of diamond [15].

Table 2.2: The ranking of various catalysts that are used in the growth of diamond. (After ref [15]).

Rank	Nucleation	Growth	Transition	All
1	Cr	Ir	Fe	Co
2	Fe	Ni	Co	Ir
3	Tc	Co	Ir	Mn
4	Co	Os	Os	Ni
5	Mn	Rh	Ni	Cr

This table represents the catalytic power of the catalysts for the graphite → diamond transition under higher pressure. The nucleation is the ability of the metal to pucker graphite and begin the process of forming diamond, the growth index is the power of the molten metal to grow diamond while the transition index is a measure of how efficiently a metal can aid in the transformation from graphite to diamond [15]. Also, the final quantity is the all-merit index, which normalizes the transitional index to the melting point of the metal.

The samples (large type Ib yellow diamonds) in this study have been grown using iron/cobalt solvent/catalyst and following the temperature gradient growth technique. This involves 'indirect heating' with the carbon source which is a fine diamond powder, separated from the solvent and the seed crystal as seen in Figure 2.7.

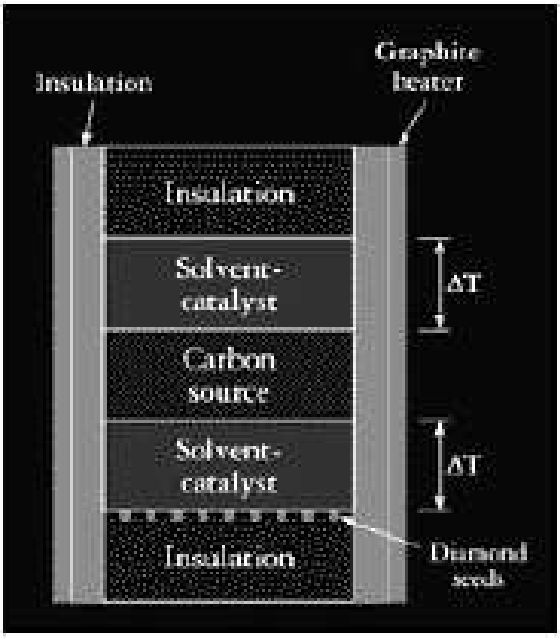


Figure 2.7: The diagram of the capsule for growing large diamonds. There is usually a temperature difference of about 30°C between the centre of the capsule and the seed pad (After ref [40]).

The growth temperature lies between the melting point of the solvent/catalyst/carbon system and the diamond-graphite equilibrium temperature [41]. A temperature gradient exists between the carbon source and the seed which drives carbon from the higher temperature region (T_2) to the cooler seeded region (T_1) where it precipitates homoepitaxially on the diamond seed [15, 41].

2.2.6 Some applications of Diamond

Being the hardest material known, diamond (CVD) is applied as an abrasive and as coating or cutting tool and as wear-resistant coating on other devices [42]. The higher thermal conductivity of diamond means that it can be used in heat sink components [22]. The negative electron affinity is well used in diamond-based field emitters [43]. Having a high speed of sound (1.96×10^5 cm/s) and a high phase velocity, the use of Diamond Surface Acoustic Waves (SAW) devices allows working at much high frequencies (2 GHz to 10GHz) than the conventional SAW [44]. Diamond-based electronics could potentially offer everything that silicon currently offers as well as excellent heat conduction, this could potentially mean that CPUs in computers could become faster as one of the major limiting factors in CPU speed is the heat transport problem [22]. The high resistivity ($>10^{15} \Omega$ .cm) of diamond at room temperature eliminates the necessity of reverse polarized p-n junctions which are essential in semiconductor detectors in order to avoid thermally generated dispersion currents, where such currents and their fluctuations are in fact an undesirable source of noise and can reduce the amplitude of the applied electric field [44]. Diamond is also applied in harsh environments due to its chemical inertness [12].

2.2.7 The doping of Diamond

The use of diamond as a semiconductor material for electronic and optoelectronic applications requires controlled doping, with both acceptors and donors. The p-type doping has been achieved where boron is an effective acceptor which fits well into the diamond lattice [45]. The n-type doping of diamond has been found to be more problematic [22] in the sense that, while substitutional boron atoms form acceptor centres in diamond situated at 0.37 eV above the valence band maximum [46], substitutional nitrogen atoms form donor centres in diamond, but they are situated at 1.7 eV below the conduction band minimum [47], too deep to provide an adequate supply of electrons within the conduction band, at room temperature [48]. Vavilov [49] found that both lithium and sodium produce active n-type doping but with the donor behaviour vanishing after annealing. Sulphur and phosphorus are not easily incorporated into the diamond lattice and cause distortions [22]. Moreover, the only well established donor state in diamond is due to interstitial phosphorus which contains a level too deep (0.52 eV) for most practical applications [50, 51]. Although phosphorus donors lie shallower than the nitrogen donors, the conduction caused by phosphorus donors at room temperature is still very poor [52]. One of the reasons why n-type diamond is so difficult to achieve may be the deterioration of electric conduction due to the incorporation of hydrogen in the doped films and/or the presence of crystalline imperfections [12]. Thus, what is urgently required, and sought for at present, is a donor with an activation energy of the same order of magnitude as that for the boron acceptor, or preferably even smaller [2].

2.3 Energy-loss mechanisms

The following compilation about the energy-loss mechanisms has been done, mainly, after Dresselhaus et al. [7].

An energetic ion penetrating into any solid loses its energy through scattering events involving the coulomb interaction of the ion with the atoms and electrons in the target. This energy loss determines the final penetration of the projectile into the solid and the amount of disorder that is created in the lattice. The slowing down process of an ion in a solid can thus be roughly divided into two dominant mechanisms for energy loss by incident ions. These are electronic energy loss, involving the interaction between the incident ions and electrons of the host material, and nuclear energy loss, involving the interaction between the incident ions and the atoms of the host material. The energy dE lost by an ion traversing a distance dx is given by

$$\frac{dE}{dx} = N \int T d\sigma \tag{2.3.1}$$

where dσ denotes the collision cross section, T is the energy lost by the ion in the course of a collision event and N is the density of scattering centres of the host material. Rearranging equation 2.3.1 give the stopping cross section, which is expressed as,

$$\varepsilon = \frac{1}{N}\frac{dE}{dx} \int T d\sigma \tag{2.3.2}$$

The total stopping power can thus be written as

$$\frac{dE}{dx} = \left(\frac{dE}{dx}\right)_e + \left(\frac{dE}{dx}\right)_n = N(\varepsilon_e + \varepsilon_n) \tag{2.3.3}$$

where ε_e and ε_n are the electronic and nuclear stopping cross section, respectively.

The cross section for the ion-nucleus interaction is given by the simple Rutherford scattering cross section i.e.,

$$\frac{d\sigma}{d\Omega} = \left(\frac{Z_1 Z_2 e^2}{4E}\right)^2 \frac{4}{sin^4\theta} \frac{\left\{\left[1 - \left(\left(\frac{M_1}{M_2}\right) sin\theta\right)^2\right]^{\frac{1}{2}} + cos\theta\right\}^2}{\left[1 - \left(\left(\frac{M_1}{M_2}\right) sin\theta\right)^2\right]^{\frac{1}{2}}} \tag{2.3.4}$$

The ion-nucleus interaction does not only result in the colliding ions changing directions, but also the atoms of the host material may also be significantly dislodged from their original positions, giving rise to lattice defects. The deviations in the projectile trajectory results in both lateral spread and a depth distribution of the implanted species, while the displacement of the host atoms gives rise to lattice damage.

Simple kinematic calculations show that the energies of the projectile before and after scattering, E_0 and E_1 respectively are related by equation 2.3.5, which is obtained from [53, 54].

$$E_1 = \kappa E_0 \tag{2.3.5}$$

where the kinetic factor is given by equation 2.3.6,

$$\kappa = \left(\frac{M_1 \cos\theta \pm \left(M_2^2 - M_1^2 \sin^2\theta\right)^{1/2}}{M_1 + M_2}\right)^2 \tag{2.3.6}$$

and the scattering angle is given by

$$\cos\theta = \frac{1 - \left(1 + \frac{M_2}{M_1}\right)\left(\frac{T}{2E_0}\right)}{\sqrt{1 - \frac{T}{E_0}}} \tag{2.3.7}$$

Here M_1 and M_2 are the masses of the projectile and target atoms, respectively, θ is the scattering angle of the projectile in the laboratory frame of reference, while T is the recoil energy transferred from the projectile to the target, which is determined from the conservation of energy , i.e.,

$$T = E_0 - E_1 \tag{2.3.8}$$

In the ion-electron interaction $\theta \sim 0^{\circ}$ and the maximum recoil energy is

$$T_{max} = \frac{4mE_0}{M_1} \tag{2.3.9}$$

in which m and M_1 are the masses of the electron and the ion, respectively.

The ion-electron interactions induce small losses in the energy of the incoming ion as the electrons in the host atoms are excited to higher bound states or to ionization states and do not produce significant deviations in the projectile trajectory. From the energy loss, the ion range R can be calculated according to equation 2.3.10,

$$R = \int \frac{dE}{dE/dx} \tag{2.3.10}$$

where the integration limits are from the initial ion energy to zero. From knowledge of the energy transferred to the electrons and to the lattice, the energy of the incoming ions can be calculated as a function of distance along their trajectory E(x). Figure 2.8 gives the dependence of the nuclear and electronic energy loss on the energy of the projectile, in the case of the implantation of carbon ions into diamond.

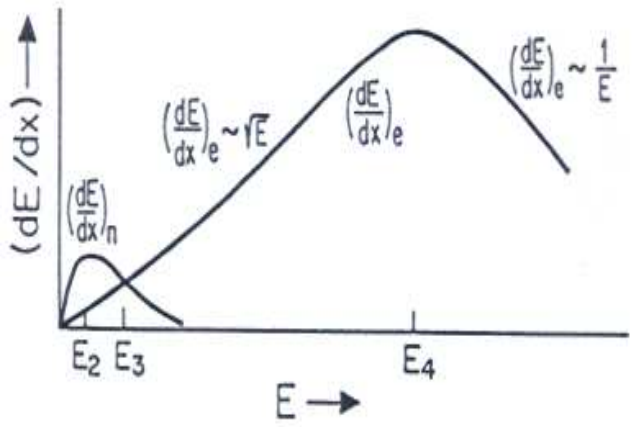


Figure 2.8: Dependence of the nuclear and electronic energy loss (stopping power) on the energy of the projectile, in the case of the implantation of carbon ions into diamond (After ref [7]).

At low energies of the projectile ion, nuclear stopping is dominant due to the $1/E^2$ dependence of the Rutherford cross section as shown in equation 2.3.4

while electron stopping dominates at high energies, as shown in the characteristic stopping power curves of Figure 2.8.

Three important energy parameters are indicated in Figure 2.8 for the implantation of carbon into diamond. The energy where the nuclear stopping power is a maximum is E_2 and is < 5 keV, the energy where the electronic stopping power is a maximum is $E_4 \approx 2$ MeV, and the energy where the electronic and the nuclear stopping powers are equal is $E_3 \approx 15$ keV. Note that only in the energy regime in which nuclear stopping dominates are the host atoms severely dislodged. Thus, nuclear stopping is responsible for most damage which accompanies ion implantation [55]. Electronic stopping will usually not create extensive damage to the host crystal, except in those cases for which electronic excitation and bond breaking are possible, so that some structural rearrangement may take place.

The slowing down processes of an ion in an amorphous solid is a statistical process. Thus the locations at which the implants finally come to rest are also of statistical nature, and should be expressed using statistical variables. Considering the projected range distribution, the Gaussian approximation gives the implant density N(x) as

$$N(x) = \frac{\Phi}{\sigma_p \sqrt{2\pi}} \exp\left[- \frac{\left(x - R_p\right)^2}{2\sigma_p^2} \right] \tag{2.3.11}$$

where x is measured along the direction of the beam, Φ is the fluence or the ion dose, while σ_p is the standard deviation in the projected range R_p (also referred to as the ion range straggling) as highlighted in Figure 2.9.

The projected mean range R_p defines the peak position measured from the target surface or gives the mean penetration depth of the ion relative to the surface while ΔR_p gives the half-width at half maximum of the implant distribution [7, 56].

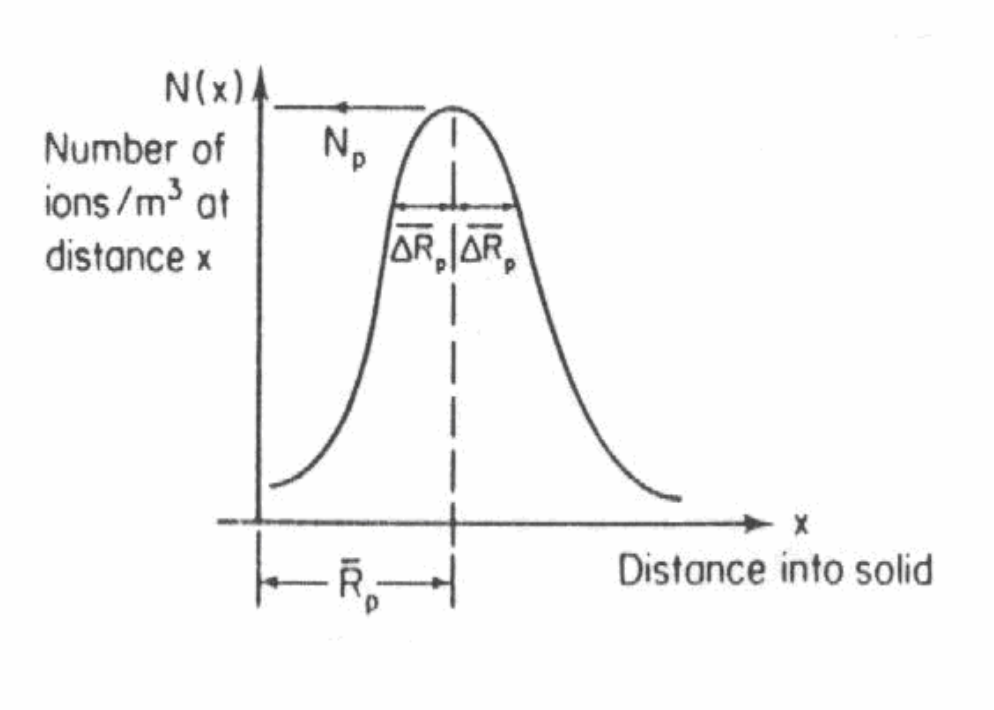


Figure 2.9: Gaussian distribution of implanted ions (After ref [57]).

The implantation process will have as its target either a crystalline or an amorphous target. In the latter case, the Gaussian distribution described will be expected. The same applies in the case of the crystalline target, with an important exception: in a crystalline target, the orientation of the target crystal becomes very important. When oriented in certain ways, there is a path for the implanted ions to travel much deeper into the substrate than desired, an effect called 'channelling'. This condition is generally handled easily by orienting the target crystal in a direction that will not lead to channelling [57].

This Gaussian approximation is useful for gaining a simple physical picture of the implant profile. It should be noted that the profile given by equation 2.3.11 ignores diffusion which may take place during the implantation and higher order effects, as well as channelling. Thus, more realistic information about the

implant distribution in the target and the related damage inflicted is obtained from computer simulation [7].

2.4 Radiation Damage

The energy transferred from the projectile ion to the target atoms is usually sufficient to break a chemical bond and to cause a displacement of the target (carbon) from its original lattice site [7]. For this to happen, the energy transferred from the projectile ion to the target atom must be greater than the displacement energy. The displacement energy (E_d) is defined to be the minimum energy necessary to permanently remove an atom from its initial lattice position [58]. It is also well known that a single incident ion may dislodge multiple-host atoms which, in turn, might displace other atoms. Thus the slowing down of a single implanted ion in the solid usually initiates a whole cascade of atomic displacements; hence the term 'damage cascade' which is used to describe this process [7]. Note that, whilst these dynamic effects are transient, the perturbed structures may re-order into characteristic arrangements of atoms to include vacancies, interstitials and simple complexes such as Frenkel pairs (i.e a pair formed by a vacancy and an interstitial) as well as dynamic crowdion which describes an ion that has been inserted into a normal row of atoms and produces a perturbation over several lattices sites [59] as shown in Figure 2.10.

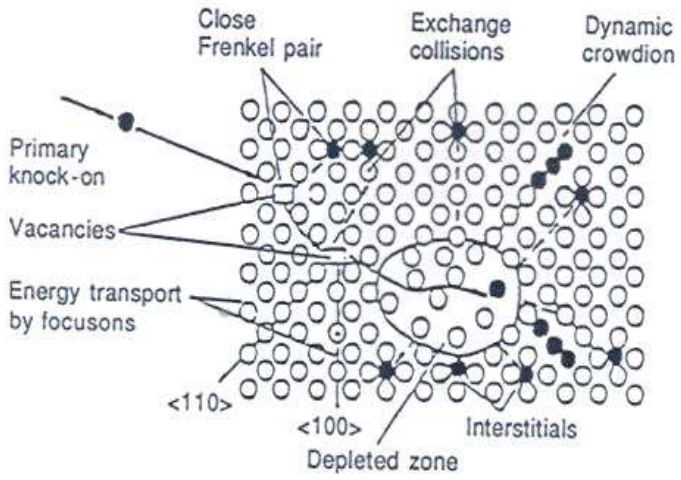


Figure 2.10: Example of typical defects by ion implantation (After ref [7]).

The agglomeration of point defects forms defect complexes, generally called extended defects which include among others dislocations loops and stacking faults. Most of the radiation effects, for example radiation embrittlement and void swelling, are deleterious to the performance of the material: hence the term radiation damage [3]. Thus, radiation damage can be defined as disorder introduced by ion implantation [59]. It should be noted that radiation damage does not necessarily have adverse effects on the properties of materials [60]. Indeed, it may frequently be avoided or removed by a suitable choice of temperature of a solid during or after implantation [59]. Thus, radiation damage can be entirely beneficial and can produce the property changes required and it is unfortunate that the phrase 'radiation damage' is used, which implies an unwanted effect [59].

2.4.1 Point defects

Point defects in diamond are inherent to the equilibrium state and thus determined by temperature, pressure and composition of a given system [60]. Point defects in diamond as shown in Figure 2.11 include primarily the substitutional defect (a defect which replaces a host atom with a foreign impurity), interstitial defect (either native or foreign and consists of an atom displaced from its normal site), vacancy (an absent host atom) and defect complex (a defect consisting of more than one atom [15], for example split-interstitial, crowdion amongst others).

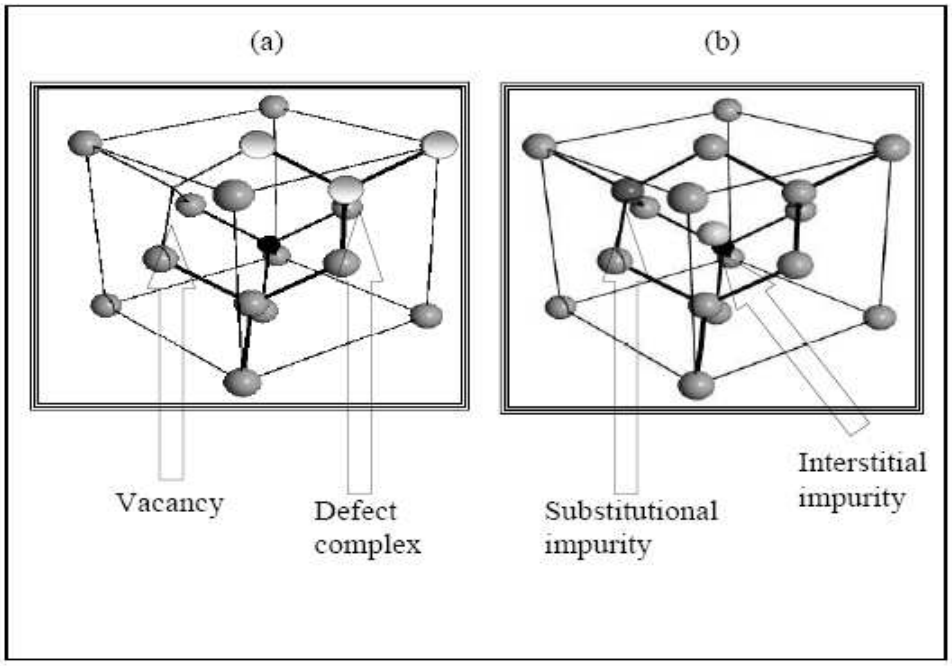


Figure 2.11: Different types of point defects in diamond (After ref [15]).

Vacancies are important in that they control the rate of matrix (or substitutional) atom diffusion-i.e., atoms are able to move around in a crystalline solid primarily because of the presence of vacancies [60]. An example of a much known defect complex is the <100>-split-interstitial ('dumbbell') as shown in figure 2.12 where two atoms share a single atomic site. According to both experiment and theory, this defect is the most stable configuration obtained during ion implantation [58, 61, 62].

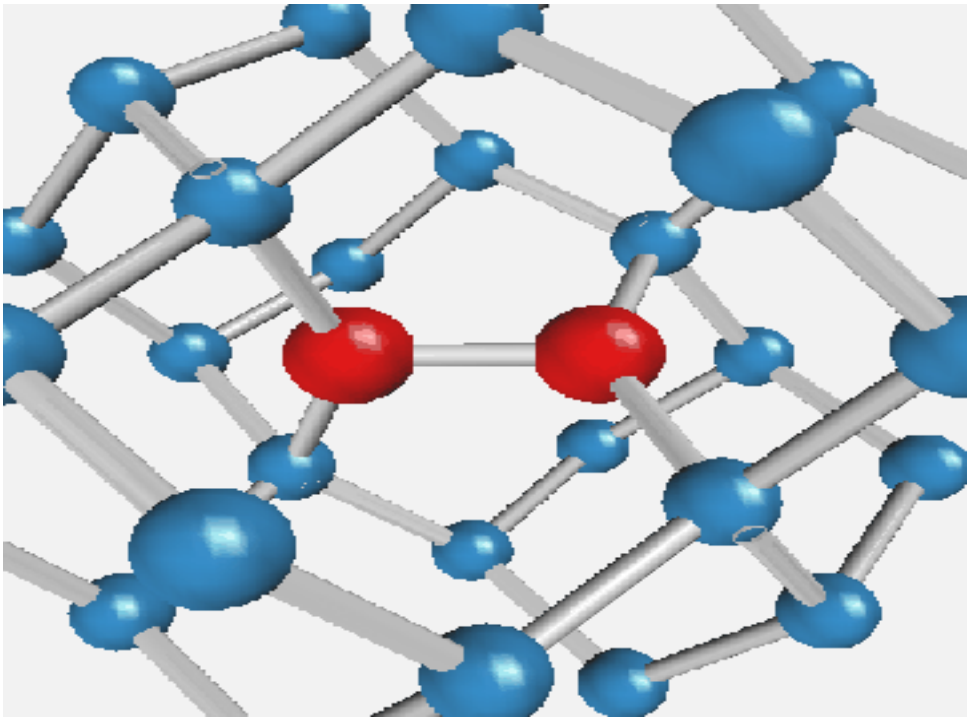


Figure 2.12: Structure of the <110>-split interstitial, showing the two atoms (in red) forming the interstitial pair, and their neighbours (in blue) (After ref [63]).

2.4.2 Line defects

Line imperfections or dislocations in crystalline solids are non-equilibrium defects that produce lattice distortions centred about a line [60]. The direction and magnitude of the lattice distortions is expressed in terms of a Burgers vector b [64]. There are two basic types of dislocations in crystalline materials namely the edge dislocation and the screw dislocation as depicted schematically in figure 2.13.

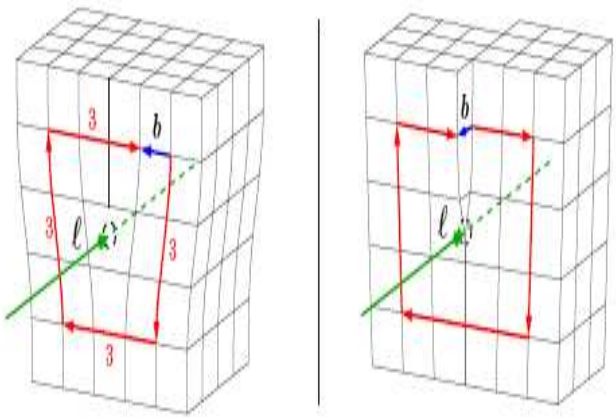


Figure 2.13: Edge and Screw dislocation in a simple cubic lattice (After ref [65]) The panel on the left hand side shows an edge dislocation while the right side one shows a screw dislocation. In these diagrams, l is the line direction, b is the Burgers vector defined by the closure fault of the Burger circuit (in red).

An edge dislocation can be visualized by inserting a half-plane of lattice sites into the crystal. Figure 2.13 shows that the dislocation line is the line where the half-plane terminates [65]. In this case the Burgers vector is perpendicular to the line direction. The screw dislocation on the other hand can be constructed by shearing one part of the crystal with respect to the other part at a half-plane only [65]. The dislocation line is also given by the line where the half-plane terminates.

A key feature of the screw dislocation is that the Burgers vector is parallel to the line direction.

The sideways motion of a dislocation is known as slip, while the plane along which it moves is the slip (or glide) plane, and the direction in which the dislocation moves is called the slip direction, which happens to be the line of the closest atomic packing [[59],[66]]. The combination of slip direction and slip plane forms the entire slip system [67]. In diamond, {111} <110> is considered as the slip system meaning that perfect dislocations lying on {111} planes possess <110> Burgers vector and the corresponding line directions [[68],[69],[70] ,[71]]. Thus, the four {111} planes are the slip planes, and as each plane contains three <110> directions, there are altogether 12 slip systems [72].

The motion of dislocations is governed by two basics types i.e dislocation glide and dislocation climb. Glide is defined as the motion of a dislocation along a slip plane containing both the dislocation and its Burgers vector [72]. For a dislocation with an edge component, this motion is restricted to the single plane defined by the Burgers vector and the line direction. An edge dislocation is only able to glide on this specified slip plane by breaking and forming new bonds [[65],[72] as shown in figure 2.14.

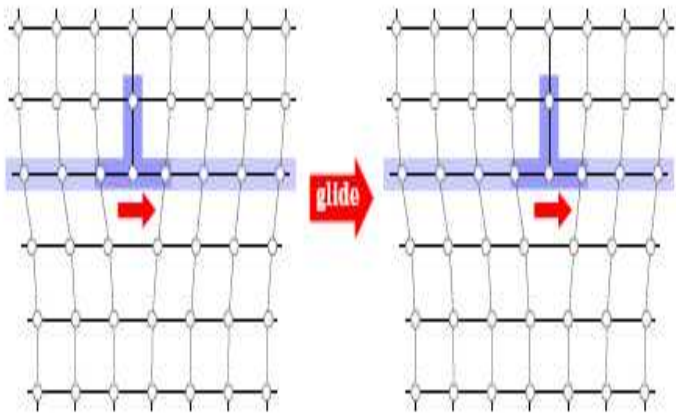


Figure 2.14: Dislocation glide in a simple cubic lattice (After ref [65]).

For dislocations with a screw component, this motion is not restricted to a single plane meaning that a screw dislocation can glide in any slip planes that have a common slip direction. This gliding from one slip plane to another, which is known as cross-slip, enables screw dislocations to bypass obstacles to their motion [72].

An edge dislocation can only avoid obstacles by moving normal to the slip planes, such as through the 'climbing' process. During this process, the dislocation moves from one glide plane to another where the direction of motion points exactly along the inserted half-plane. In this case, the half-plane either shrinks following an upward climb as shown in figure 2.15, or it expands following an downward climb [65].

During the climb process, absorption or creation of lattice sites occurs. In a real crystal, this can be achieved through the release or trapping of either interstitial atoms or lattice vacancies [65].

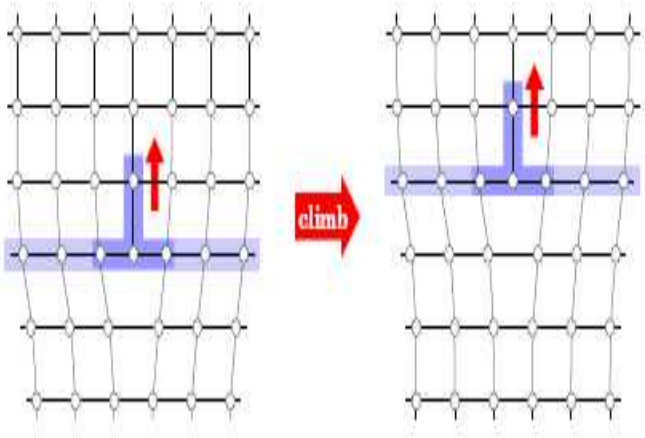


Figure 2.15: Dislocation climb in a simple cubic lattice (After ref [65]).

2.4.3 Planar defects

Planar defects or surface defects are the boundaries, or planes, that separate a material into regions, each region having the same crystal structure but different orientations [67]. Some of these defects include grain boundaries, twin interfaces and stacking fault among others.

A grain boundary is a non-equilibrium defect that may be defined as the interface between crystals that differ in crystallographic orientation, composition or dimensions of the crystal lattice (in some cases in two or all of these) [72]. In a grain boundary, the atoms are so close at some locations that they cause a region of compression, and in other areas they are so far apart that they cause a region of tension [67]. A low or small angle grain boundary consists of an array of dislocations between adjoining crystals grains as suggested by Burgers [66], and illustrated in figure 2.16. It is produced by an array of dislocations, causing an angular mismatch θ between the lattices on either side of the boundary. Here, D=b/θ , where D is the spacing and b is the Burgers vector.

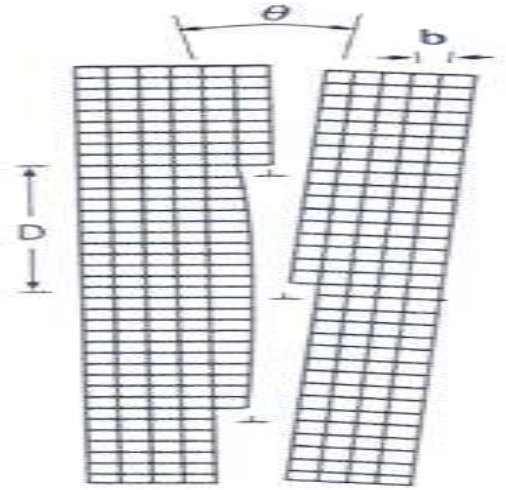


Figure 2.16: Small angle grain boundary (After ref [67]).

It is noteworthy to mention that small angle boundaries formed by edge dislocations are called tilt boundaries whereas those caused by screw dislocations are called twist boundaries [67].

A crystal is twinned when one portion of the lattice is a mirror image of the neighbouring portion, the mirror image being the twinning plane [72] as shown in figure 2.17.

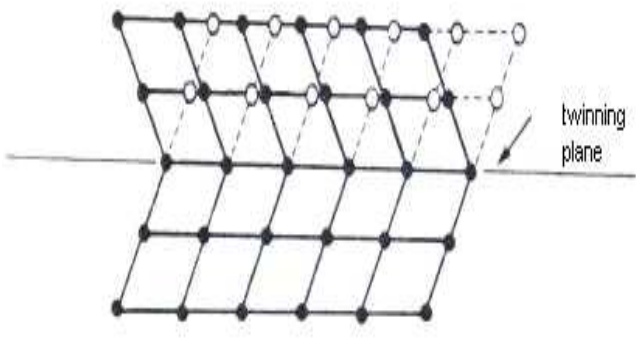


Figure 2.17: The arrangement of the atoms on either side of a twin interface (After ref [72]).

A stacking fault is defined as a plane within the crystal structure where atomic planes are suddenly displaced by a fraction of the interatomic spacing [73].

Twin boundaries and stacking faults interfere with the slip process but the high-energy grain boundaries are much more effective in blocking dislocations than either stacking faults or twin boundaries [67].

2.4.4 Other defects

According to Townsend et al [59], if a high vacancy concentration is produced in a solid there is a tendency to form large empty volumes, or voids while if there is a gas contained within these volumes, then they are referred to as bubbles. They also say that blistering occurs if bubbles diffuse to the surface allowing the internal gas pressure to cause them to burst and some fragments of the surface are removed. They conclude by stressing that such problems may not seem relevant to normal implantation work except in the simulation of reactor damage, however, blistering does occur under certain circumstances even if small quantities of implanted material are involved.

Chapter 3

Experimental Techniques

3.1 Layout of the Chapter

This chapter outlines the experimental techniques used in this study. The first section discusses the ion implanter used in creating the desired damage. It presents also the ion mill and the transmission electron microscope and associated analytical techniques used to thin the samples down to electron transparency and to characterize the samples respectively while the second section discusses the specimen preparation techniques.

3.2 Equipment used

3.2.1 The Ion Implanter

This study involved mainly the study of damage (defects) caused by ion irradiation on diamond. For this reason, an ion implanter model 200-20AF [74] was used. This implanter was specifically designed as a production tool for the manufacturing of ion implanted, semiconductor devices at high doping levels but has been modified to be able to be used for research implantations. It employs electrostatic beam scanning of individual wafers, this ensuring uniform irradiation. Figure 3.1 highlights different parts of the Ion Implanter.

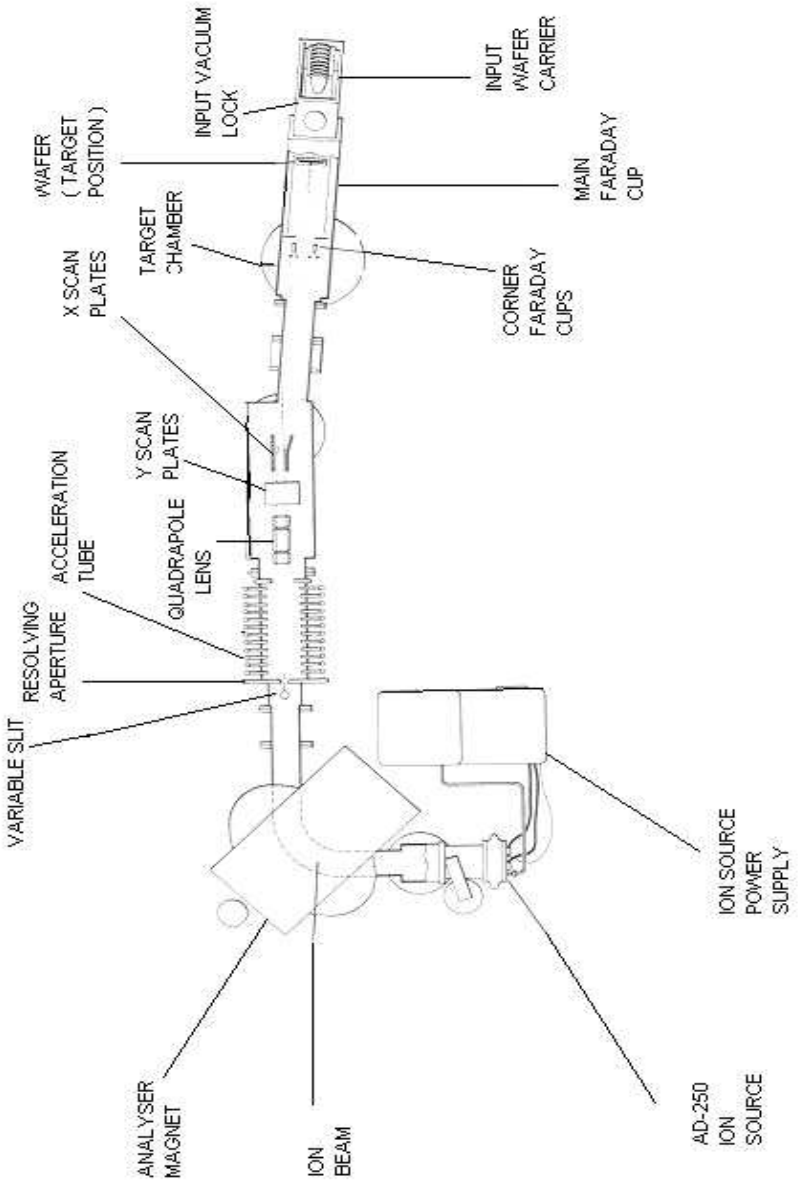


Figure 3.1: A schematic diagram of the model 200-20AF Ion Implanter. (After ref [74]).

Its operational principles are as follows:

A beam of ions which is generated by the hot cathode arc discharge ion source is extracted from the source by the electrostatic field set up between the source exit aperture and the extraction electrode. These ions are then accelerated to an energy of 25keV and admitted to a 90° double-focusing analyzing magnet provided for beam resolution, focusing and analysis, in the high voltage terminal.

The magnet current is adjusted so that only ions with the atomic weight of the particular species desired will follow a path through the magnet and be focused at the image point of the analyzer. All the other ions in the beam will follow paths depending on their mass and energy and will be collected on the analyzer chamber walls or on either side of the resolving aperture which is located in the image plane. The resolving aperture has a diameter such that only the ion beam of the species desired will pass through.

The ion beam further passes through a variable slit, located immediately before the resolving plane. The intensity of the beam is controlled by opening and closing the slit.

On emerging from the analyzing aperture, the ion beam enters the acceleration tube designed to optimize beam focusing and minimize X-rays generated by electron backstreaming, whose upstream end is at high voltage terminal potential, and whose downstream end is at ground. The field in the acceleration tube provides the main acceleration of the ion beam, which emerges with an energy of between 25-200 keV. The tube has very little focusing action, so the beam diverges as it passes through the accelerating region until it reaches the lens located at the entrance of the scanner box. The lens is an electrostatic quadrupole triplet which is used to focus the beam to a small symmetrical spot in the target chamber.

After passing through the lens, the beam, now convergent, enters the deflection region where electrostatic deflection plates first deflect the beam in the vertical (Y) plane and then in the horizontal (X) plane. These deflection plates are used to scan the beam across the surface of the wafer in a non-repeating raster pattern so as to cover the wafer uniformity.

Finally, the focus beam current is measured directly in a deep Faraday cup before the implant. In addition, four small holes of 0.24 cm^2 each, located near the extremities of the scanned beam, allow the beam to be sampled during the implant by four Faraday cups mounted immediately in front of the wafer. In addition, the current registered by each of the four Faraday cups may be used to check the scan uniformity during the implant.

3.2.2 The Ion Mill

The ion mill used is the Model 691 Gatan Precision Ion Polishing System (PIPS). It is an excellent tool designed for producing a high quality TEM specimen. The basic principle of ion milling involves bombarding a specimen slice with energetic ions or neutral atoms accelerated and formed into a tightly focused ion beam[75]. Material is then sputtered from the specimen down to electron transparency within the area of interest.

In order to appreciate the polishing process, a schematic illustrating the PIPS work chamber is shown in Figure 3.2. It consists mainly of two miniature Penning ions guns (PIGs), Specimen Airlock, Viewing Microscope and a specimen post. The rôle of the two miniature Penning ions guns is to deliver powerful and stable ion beams. The Specimen Airlock makes it easy to load and unload specimens from the PIPS for periodic inspections under a high optical microscope during the final moments of the thinning process. The microscope used in this case is powerful enough to resolve interference fringes and can also be used to monitor the thinning of the specimen directly [76].

Finally, the single side specimen post was originally designed to facilitate low angle milling in the model 600 Duo Mill and whose purpose was to [76]:
(1) minimize contamination materials sputtered from the specimen holder.
(2) reduce beam heating by providing an excellent heat sink right next to the thinnest area of the specimen and
(3) facilitate specimen handling.

Ion milling is a slow process in hard materials. In order to apply it to the diamond specimens, it was first necessary to reduce their thickness to about 40μm by mechanical thinning techniques, as described in Section 3.3.1.

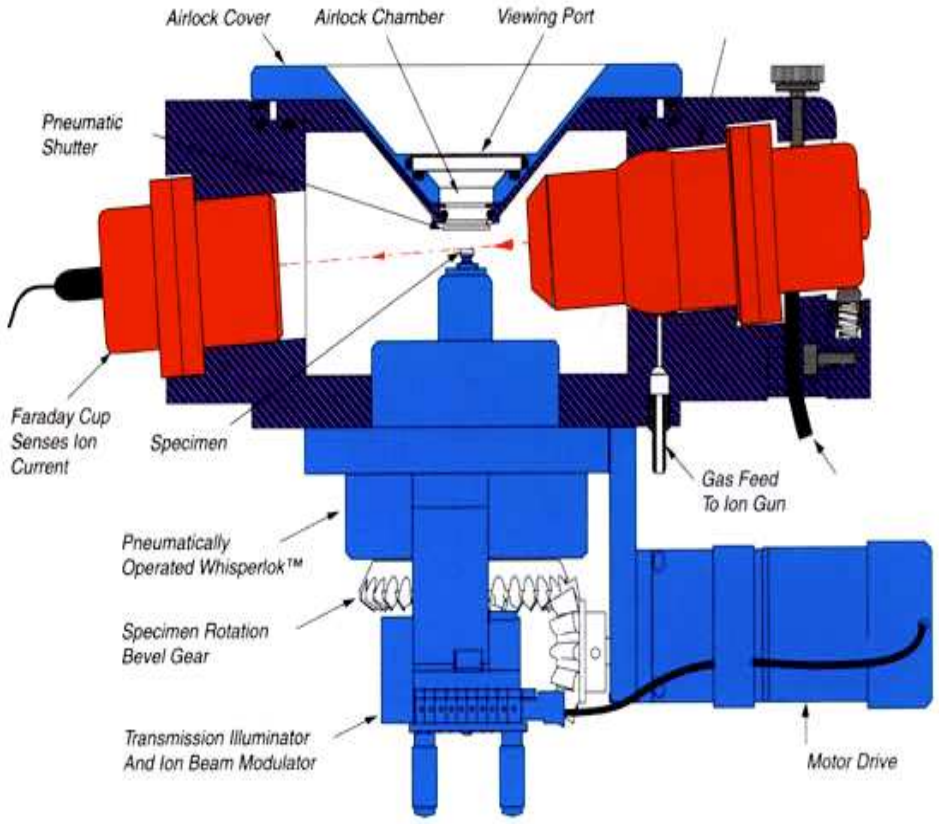


Figure 3.2: A schematic illustration of the PIPS work chamber showing the Penning Ion gun, the specimen exchange mechanism, the Faraday cup, the airlock and the specimen post. (After ref [76]).

3.2.3 The Transmission electron Microscope

When accelerating electrons up to high energy levels (few hundreds of keV) onto a thin specimen as used in TEM, they can scatter or backscatter elastically or inelastically, or produce many interactions, sources of different signals such as X-rays, Auger-electrons, light among others [65, 77] as shown in Figure 3.3. Signals above the specimen i.e. X-rays, Auger-electrons, light, backscattered electrons are used when examining a thick specimen with the aid of a Scanning Electron Microscope (SEM) while signals below the specimen i.e. incoherent elastic scattered electrons, incoherent inelastic scattered electrons are utilized in thin specimens via the Transmission Electron Microscope (TEM).

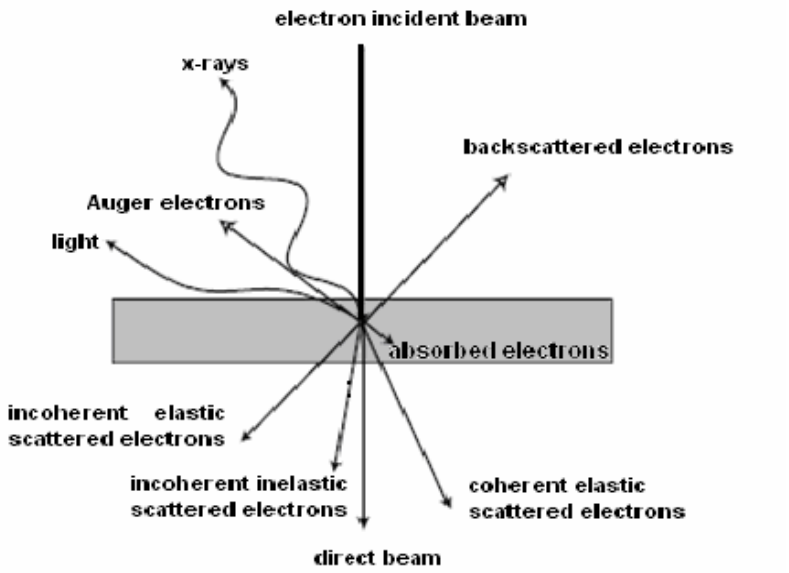


Figure 3.3: Interaction between electrons and material. (After ref [77]).

The description of the conventional Transmission Electron Microscope [78] is as follows:

A modern transmission electron microscopy (TEM) is composed of an illumination system, a specimen stage, an objective lens system, the magnification system, the data recording system(s), and the chemical analysis system as shown in figure 3.4.

The electron gun is the main component of the illumination system, which typically uses a LaB_6 thermionic emission source or a field emission source.

The LaB_6 gun gives a high illumination current, but the current density and the beam coherence are not as high as those of a field emission source. The field emission source is unique for performing high coherence lattice imaging, electron holography, and high spatial resolution microanalysis. The illumination system also includes the condenser lenses that are vitally important for forming a fine electron probe.

The specimen stage is key to carrying out structure analysis, because it can be used to perform in situ observations of phenomena induced by annealing, electric field, or mechanical stress, giving the possibility of characterizing the physical properties of individual nanostructures. The objective lens on the other hand determines the limit of image resolution, and therefore key to the TEM process. The magnification system consists of intermediate lenses and it gives a magnification up to 1.5 million. The data recording system is often digital and the use of a charge coupled device (CCD) allows for quantitative data processing.

Finally in the chemical analysis stage both energy-dispersive X-ray spectroscopy (EDS) and electron energy loss spectroscopy (EELS) are used in a complementary way to quantify the chemical composition of the specimen. Moreover, while EDS relies on the counting of X-rays emitted from the beam-illuminated specimen region as a function of the photon energy, EELS analyzes

the intensity distribution of the transmitted electrons as a function of their energy loss. The latter is extremely important because it not only provides the chemical information on the specimen but also its electronic structure.

When the entrance surface of a thin foil specimen is illuminated by a parallel or nearly parallel electron beam, the latter is diffracted by the lattice of the crystal, forming Bragg beams which then propagate along different directions [77].

In this case, it is important to note that elastic scattering [65] in a crystal occurs with highest intensity whenever the Bragg condition for diffraction is met as shown in figure 3.5.

$$n\lambda = d_{hkl} \sin\theta, n = 1, 2, 3, ... \tag{3.2.1}$$

where λ is the wavelength of the electron beam, d_{hkl} the spacing of a set of (hkl) crystallographic planes and θ gives the angle between the beam and a set of planes. Also, in the vicinity of a structural defect such as a dislocation, the lattice is strained and the lattice planes are bent locally resulting in local changes of the Bragg condition and thus in a change in intensity of the diffracted and transmitted beams [65].

The imaging mode can be done in two ways as seen in figure 3.4. These are the bright and the dark field modes. The bright field mode BF entails masking all diffracted beams by the objective aperture and hence only the transmitted beam is used for imaging process. The dark field mode DF on the other hand involves selecting one of the diffracted beams by tilting the incident beam so that the diffracted beam is put on the objective lens axis [77]. as shown in figure 3.4(b). The bright field images are useful in giving a first impression of the microstructure while the dark field method which is lower in intensity

results in a better contrast than the bright field microscopy [65].

Figure 3.4 shows the selected area aperture situated between the objective aperture and the intermediate lens, and its rôle is to select only one part of the imaged specimen. This mode is called selected area diffraction or SAD.
In this mode, the spherical aberrations of the objective lens limit the area of the selected object to few hundred nanometers. Moreover, one can obtain diffraction patterns of a smaller object by focusing the electron beam with the projector lenses to obtain an even small spot size on the object surface of between about 2-10 nm. The spots of SAD become discs whose radii depend on the condenser diaphragm and this is called micro diffraction as shown in figure 3.6.

Images obtained using TEM are usually dominated by three types of contrasts. The first is the diffraction contrast, which is produced due to the perturbation of local strain/defects/dislocations on the intensities of the Bragg reflected beams [79]. This contrast is also called amplitude or strain contrast and it is the most common mechanism used in radiation-damage studies [3]. The second is the phase contrast, which is produced by the phase modulation of the incident electron wave when it transmits through the crystal potential. This contrast is especially sensitive to the atom distribution in the specimen. The last one is the mass thickness or atomic number contrast and is most frequently performed in scanning transmission electron microscopy (STEM).

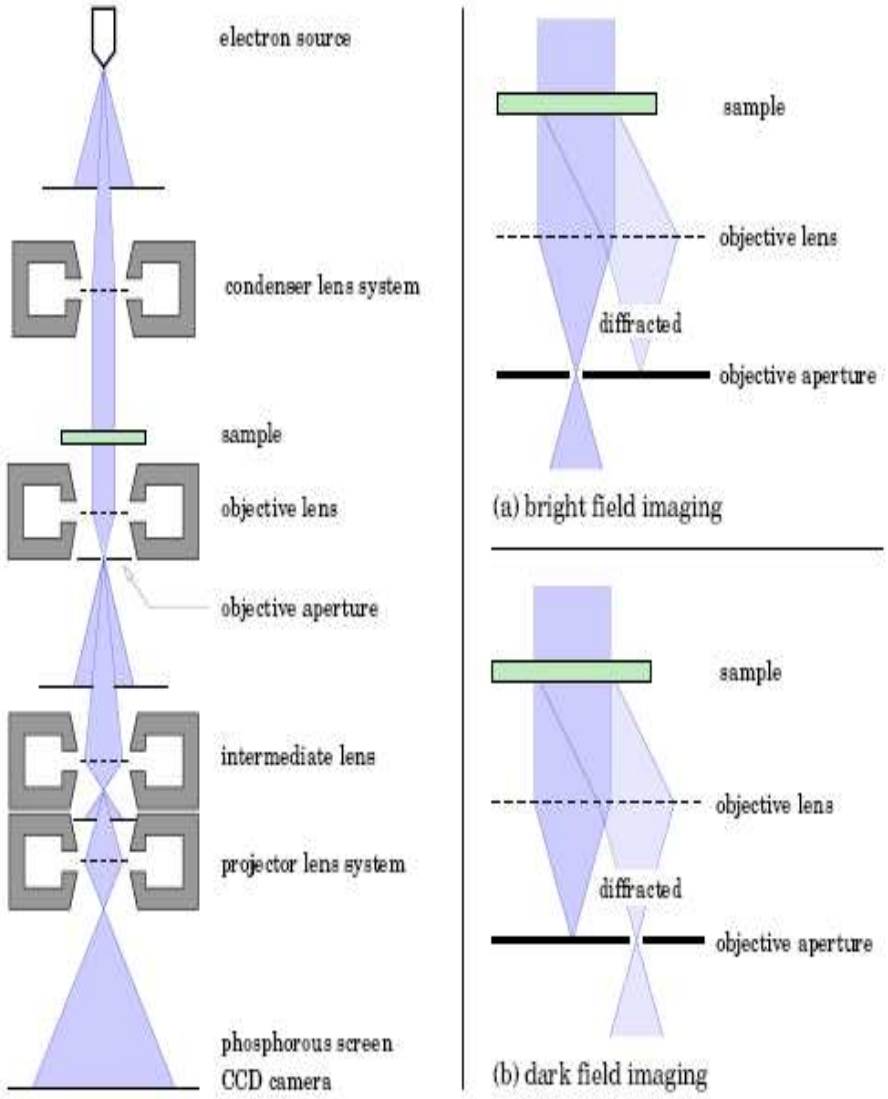


Figure 3.4: Schematic illustration of a transmission electron microscope. (After ref [78]) The panel on the left hand side shows a simplified representation of the TEM setup, while the right hand side one shows the two basic imaging modes.

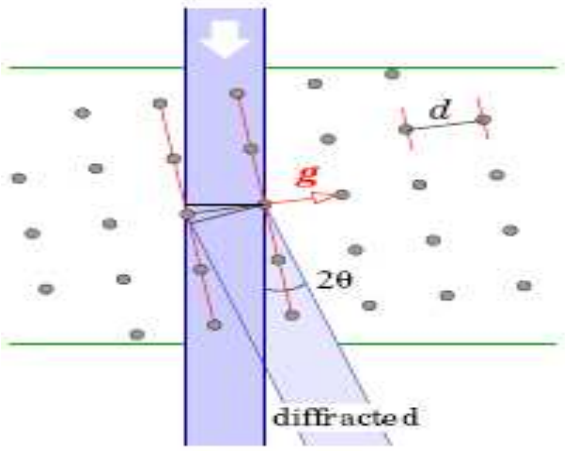


Figure 3.5: Bragg diffraction in the TEM sample (After ref [65]). g denotes the corresponding diffraction vector.

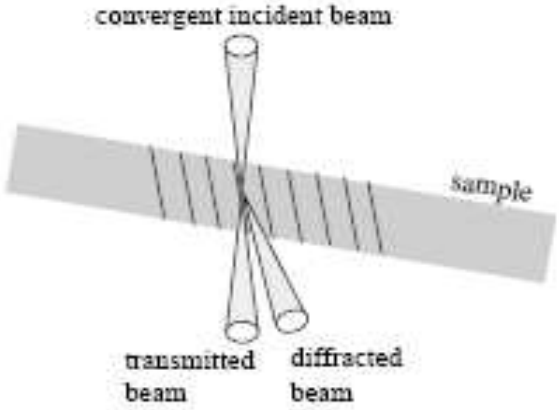


Figure 3.6: Microdiffraction mode. (After ref [77]).

Special TEM techniques include Scanning Transmission Electron Microscopy (STEM) [77], High Resolution Transmission Electron Microscopy (HRTEM) and Electron Energy-Loss Spectrometry (EELS) [80] among others.

The basic principle of image formation in the STEM is fundamentally different from that of static beam TEM. In this case, a small spot size is formed on the sample surface with the condenser lenses. This probe is then scanned on the sample surface with scan coils, and in parallel, the signal is detected by an electron detector, amplified and displayed on a cathode-ray tube (CRT) synchronously with the scan coils.

The detector is often a small disc on the column axis, which detects only the transmitted beam (BF STEM) or a diffracted beam (DF STEM). It can also be an annular detector (a plate with a hole) which detects all the diffracted beams except the transmitted ones (ADF STEM). The resolution of the image in STEM is only limited by the spot size (quality of the condenser lenses) since the objective lens is not used in this case. However, STEM images do have generally poorer resolution, which is nonetheless compensated for by better contrast than TEM images. The STEM mode [81] is quite useful in cases where high resolution images are required as well as in microanalysis, and microdiffraction at the atomic level.

While conventional TEM uses only the transmitted beams or some of the forward scattered beams to create a diffraction contrast image, High Resolution Transmission Electron Microscopy (HRTEM) uses the transmitted and the scattered beams too, so as to create an interference image [77]. In HRTEM, two or more Bragg reflections are used for imaging. This makes it possible to analyze very thin samples, since they can be treated as weak-phase objects where the image intensity can be correlated to the projected electrostatic potential of crystals, leading to atomic structural information [82].

Electron energy-loss spectroscopy (EELS) involves measuring the energy distribution of electrons that have passed through a thin specimen in a TEM, usually by adding a magnetic spectrometer beneath the viewing chamber as shown in figure 3.7. If the electron probe is scanned over the specimen and a narrow slit (followed by a single-channel electron detector) used in the spectrum plane, an energy-filtered signal is obtained.

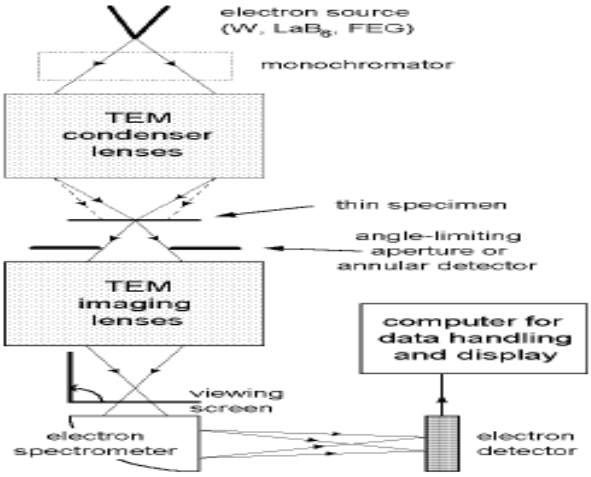


Figure 3.7: Schematic of a spectrometer system for recording energy-loss spectra and energy filtered images. Electron paths are arrowed. (After ref [80]).

Alternatively, the focusing properties of a magnetic spectrometer can be exploited to form an energy-filtered (EFTEM) image from a stationary and broadly-focused incident beam. Figure 3.8 shows a simplified energy-loss spectrum.

For very thin specimens, the most prominent feature is the zero- loss peak where the area I_o represents purely elastic scattering. The plasmon peak, due to inelastic scattering by outer-shell (valence) electrons in the specimen, is centred around a plasmon energy E_p, generally in the range between 10-30 eV. Plural scattering of the transmitted electrons gives rise to additional peaks, at multiples of E_p .

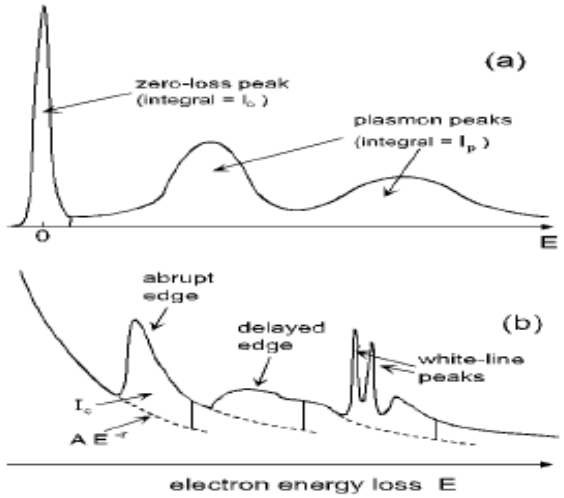


Figure 3.8: A simplified energy-loss spectrum. (After ref [80]) (a) Low-loss spectrum and (b) The core-loss region (recorded with higher detector sensitivity) showing several basic shapes of ionization edge, each superimposed on a spectral background (dashed curves).

At higher energy loss, ionization edges occur due to inelastic excitation of inner-shell (core) electrons. These are superimposed on a falling background representing the tail of lower-loss inelastic processes, which usually approximates to a power law: AE^{-r} where A and r are constants within a limited range of energy loss E. The threshold energy of each edge is the binding energy of the corresponding atomic shell and is tabulated for all elements and electron shells (K, L, M, etc.), allowing elements present in the specimen to be identified.

The energy-loss spectrum also contains fine structure, in the form of intensity oscillations or local peaks. The energy-loss near-edge structure (ELNES), in the form of pronounced peaks just above the ionization-edge threshold, can be related to chemical bonding or electronic band structure (density of states).

Extended energy-loss fine structure (EXELF), which is a weaker intensity modulation starting at 50 eV or more from the ionization edge, can be analyzed to give the distance of nearest-neighbour atoms.

3.3 The specimen preparation

X-TEM specimens must be slices cut perpendicular to the surface below which the damage is being studied. As mentioned in Section 3.2.2, the diamond slices must be reduced to about 40μm before final thinning by ion milling can be attempted. This can only be achieved by careful mechanical polishing, a process which may raise the diamond sample temperature into the annealing region. This would compromise the rapid annealing to a known temperature, which is part of the desired procedure. It is necessary therefore to polish the slices down first, then implant them into the thin edge, then anneal according to the desired regime. Fortunately the implant depth (about 0.25μm) is very much less than the specimen thickness of $\sim$ 40μm, which still appears to be a large-area specimen from the ion implantation point of view. This is illustrated schematically in Fig. 3.9

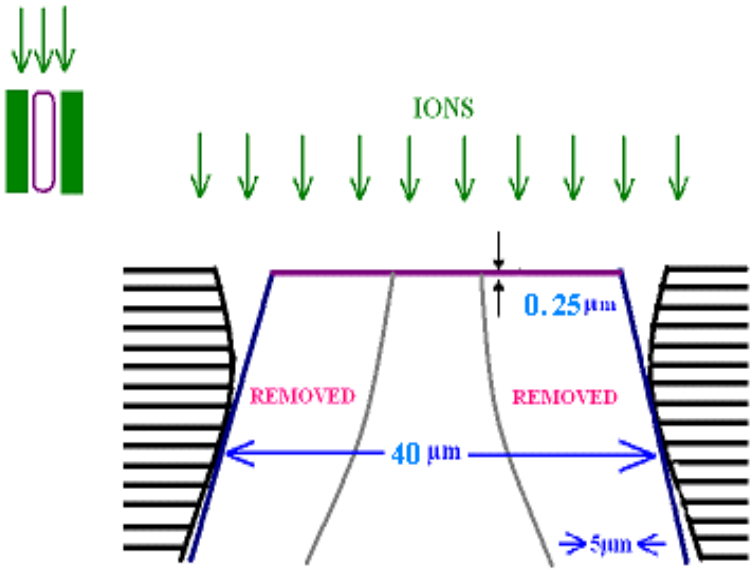


Figure 3.9: Enlarged schematic view of the diamond implant situation, to scale.

3.3.1 Mechanical Polishing

A high-pressure, high-temperature (HPHT) synthetic diamond sample was used in this study which had half octahedron shape, with a single substitutional nitrogen concentration of about 84 ppm. Its weight was 0.95 carats (ct) and it was selected carefully by Mik Rebak (Diamond Polisher) so that it was free of strains and inclusions. It was of (110) crystallographic orientation and was polished less than 2° off the principal planes.

The aforementioned synthetic diamond stone was initially laser-cut into four smaller diamonds with thicknesses of about 460μm, 420μm , 650μm and 670μm, each trapezium-shaped with dimensions 5× 2.5× 3mm, using a Nd-YAG laser. It should be noted that, to initiate cutting, the diamond's surface needed to be blackened in order to ensure coupling with the laser beam [26]. One should bear in mind also that it is essential to remove the extra graphitic layer induced through the laser-cutting process. Some of our samples were sawn using a conventional diamond saw along the <100> direction, but the sawing process was lengthier than the laser-cutting and required specialized skills.

The laser-cut samples were held into position for polishing through brazing, since their small thicknesses made it hard to use any other technique. Thermal expansion mismatch was avoided by mounting them on a large diamond, designated as 'base diamond' using three-components brazing alloy around the sample. The 'base diamond' together with the sample was heated in a vacuum furnace to the braze melting temperature of about 860°C. It is worth mentioning that the base was polished beforehand in order to have parallel faces and high surface finishing, so as to ensure good contact. Also, great care was taken by not allowing the brazing alloy underneath the sample to avoid specimen thickness measurements inaccuracy. This was done by etching off any excess dried brazing alloy that was surrounding the sample. These manipulations, and

polishing, were carried out by Mr. Mik Rebak.

The diamonds were then polished by pressing the assembly of base and sample, initially mounted in a holder, against a scaife. The scaife was made of a cast iron disc rotating at about 3000 rev min^{-1} and was used to jig and polish the sample down to around 40μm, periodically adjusting the X-directional micrometer to maintain the 'O' (X-Y direction) inclinometer setting [83, 84, 85]. In order to obtain extra-fine finish, the scaife was charged with diamond powder of just $1/10^{th}\mu$m before use and from time to time during the polishing process. Also, in order to obtain the desired thickness, the amount of the removed material was monitored throughout the polishing process via a digital, five decimal high gauge micrometer.

After the polishing, the samples were cleaned by boiling them for about 30 minutes in a three components acid, viz., one part HNO_3, three parts $HClO_4$ and four parts H_2SO_4. The cleaned diamond was then rinsed in doubled-distilled deionised water and then dried off.

Grillo SE et al [85] have shown that two distinct processes take place during diamond polishing on the {100} plane. These are the 'hard' (<110>) and 'easy'(<100>) directions. According to them, material detaches by a process of nano-fracture in the <110> direction while a model of mechanically induced transformation of diamond to sp^2 hybridized carbon occurs on the diamond surface during polishing in the <100> direction. Similarly, Jarvis et al. [86] have proposed earlier, the mechanical process of nanogrooving as the principal mechanism for wear of the {110} surface of diamond during polishing in the soft direction (<001>) while the same process is applied to the {110} surface of diamond during polishing in the hard direction (<1$\bar{1}$0>) but with more difficulties.

3.3.2 Implanting

Sub-MeV ion implantations use incident ions in the range of $\sim$ 10-300 keV to modify the property of carbon-based materials to a depth of $\sim$ 10^2-10^4 Å, making ion implantation, in this case, a near surface phenomenon [7].

In this study, singly charged carbons ions were implanted edge-on, according to the CIRA (Cold-Implantation-Rapid-Annealing) routine.

A special holder, as shown in Figure 3.10 was fabricated making it easier to mount the thin diamond sample edge-on to the incoming ion beam. The implantations (in this case multi-implantations) were performed at the liquid-nitrogen target temperature, followed by a rapid thermal annealing. It is believed that by holding the diamond samples at liquid-nitrogen temperature (77K) during implantation, the radiation damage is 'frozen in' ensuring that the interstitials remain in close proximity to the vacancies [87]. After implantation of the diamond sample, it was rapidly removed from a target holder and kept in a liquid nitrogen Dewar, while awaiting the annealing.

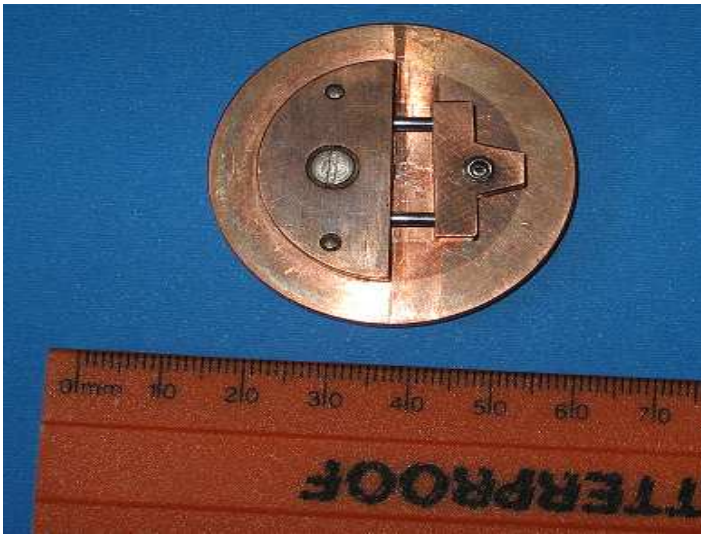


Figure 3.10: A photograph of thin diamond holder.

The multi-implantations consisted of spreading the implantation energies and doses of carbons ions as shown in Table 3.1, in order to prepare a large uniform ion-damaged depth [88].

Table 3.1: Implantations parameters. (After ref [10])

Implanted Ion	Ion energy	Low dose implantation	High dose implantation
	[keV]	[ions/cm^2]	[ions/cm^2]
		Dose component	Dose component
^{12}C	150	1x10^{15}	2.5x10^{15}
^{12}C	120	0.652x10^{15}	1.652x10^{15}
^{12}C	80	0.548x10^{15}	1.548x10^{15}
^{12}C	50	0.3x10^{15}	1.3x10^{15}
-	-	2.5x10^{15}	7.0x10^{15}

The total doses for the $^{12}C^+$ ions were 2.5x10^{15} (low dose implantation i.e below the so-called critical amorphisation threshold which is $\approx$ 5.2x10^{15} ions/cm^2) and 7.0x10^{15} ions/cm^2 (high dose implantation i.e above the critical amorphisation threshold). In addition, the dose rate for the $^{12}C^+$ was $\approx \frac{1}{3}\mu$Acm^{-2}.

It has been shown that below the critical amorphisation threshold, thermal annealing can restore the as-implanted diamond sample to a form close to its pristine state, whereas, above the critical amorphisation threshold, thermal

annealing leads to the conversion of the damaged diamond layer to graphite [89].

Note that the term 'amorphisation' describes the structural reorganisation occuring within the damaged layer [10] while the critical amorphisation threshold is defined as the dose at which thermal annealing cannot restore the damaged layer but instead results in the transformation of the latter to graphite [90]. The ion fluence (or ion dose) and the dose rate are respectively, the total number of ions incident per unit area of the target material and the rate at which the implantation occurs, often expressed in terms of the beam current density i_b in units of $\mu A/cm^2$ [7].

3.3.3 Annealing

The rapid thermal annealing (RTA) furnace used was an electrical horizontal split tube furnace (STC) with maximum tube furnace operating temperature of 1500°C as shown in Figure 3.11. It has silicon carbide heating elements which are arranged symetrically around a separate ceramic worktube to ensure excellent thermal uniformity [91].

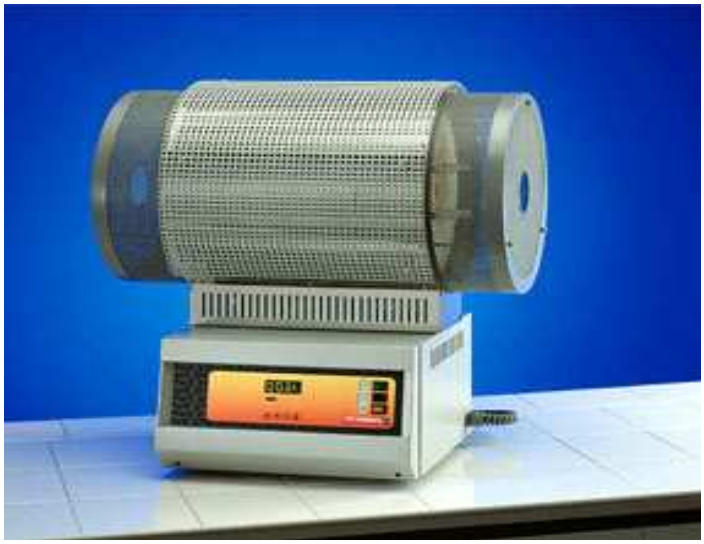


Figure 3.11: Horizontal Split Tube Furnace (STF). (After ref [91]).

A long quartz tube similar to the one shown in Figure 3.12 was inserted in the furnace and connected to a constant flow of high-purity so as to avoid an oxidising atmosphere. This effectively prevents unwanted graphitization of the as-implanted diamond sample during the annealing process. The required annealing temperature was set, and allowed to settle. Once this was achieved, the as-implanted diamond sample was swiftly removed from a liquid nitrogen Dewar (container) and then transferred into the pre-heated furnace as quickly as possible, and annealed for about half an hour, at 1600K under flowing high purity argon.

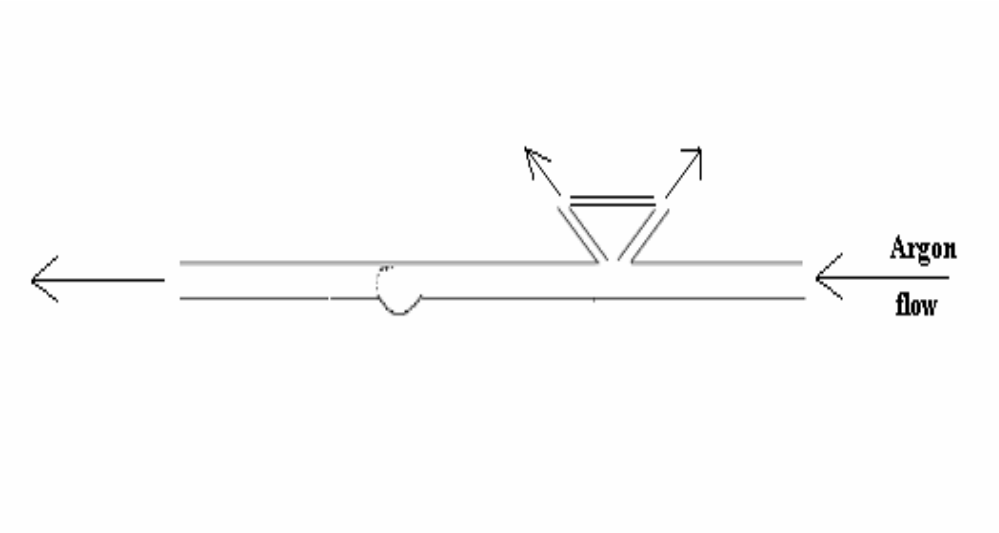


Figure 3.12: Schematic diagram of the quartz worktube. Some argon flows continuously out of the entry funnel, preventing the ingress of air.

The rapid transfer of the as-implanted diamond was made possible by blowing it in using the stream of argon gas which was already flowing through the quartz worktube. In addition, the quartz worktube was designed in such a way that the as-implanted diamond sample would be captured easily in its central bulk, i.e. precisely in the middle of the four silicon carbide heating elements.

The aim for applying the Rapid Thermal Annealing to the as-irradiated diamond samples was to preventing substantial interstitial diffusion before reaching the chosen temperature [26]. After annealing, the diamond samples were boiled in a solution of sulphuric, nitric and perchloric acids followed by rinsing in distilled water [92].

3.3.4 Ion Milling

Ion milling is a widespread final specimen preparation technique which suits cross-sectional transmission electron microscope (TEM) specimens and which thins the latter down to electron transparency.

Before applying the ion milling technique, a pair of the thin diamond slices of about 45μm (thickness) as shown in figure 3.13, had to be glued, an implanted and annealed long-edge to an unimplanted long-edge, while concurrently mounting them onto a copper support grid. Thus implanted and unimplanted samples could be directly compared.

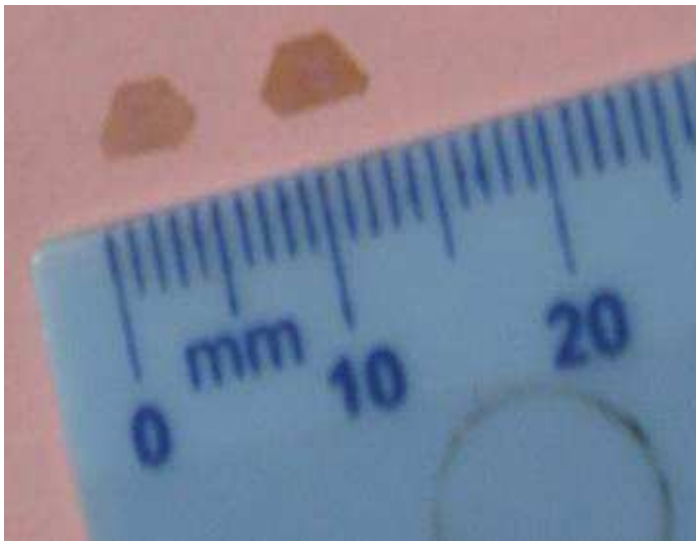


Figure 3.13: Photograph of a pair of thin slice diamond samples.

The glue used consisted of two-component Gatan epoxy which was mixed according to the standard ratio i.e. 1 hardener to 10 resin.The glued sample as shown schematically in figure 3.14 was then heated up in an oven at 100 ^{0}C for about 15 minutes for hardening.

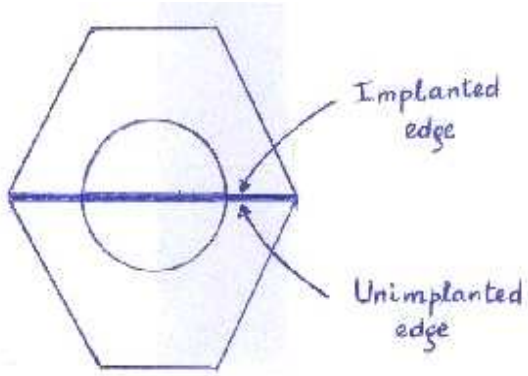


Figure 3.14: Schematic diagram of principle of preparation and mounting of diamond samples for ion beam damage studies by X-TEM.

The final specimen was laser cut out around the copper grid making sure that it fits into a shallow 3mm diameter circular disc and then argon ion beam milled to electron transparency as shown in figure 3.15. The final thinning of the sample was done by ion milling in a Gatan PIPS Ion Mill using 5 keV argon ions at an incident angle of 6 degrees with respect to the diamond sample surface. It is known that for some materials, ion bombardment carried out usually by 5-10 keV energy Ar^+ causes radiation damage of the specimen surface which could change what one wants to look at.

But fortunately, it has been demonstrated that decreasing the ion beam energy (down to 500eV) and the angle of incidence of the ion beam measured from the surface (down to 1^0) and using a liquid-nitrogen cold stage decreases the radiation damage [93].

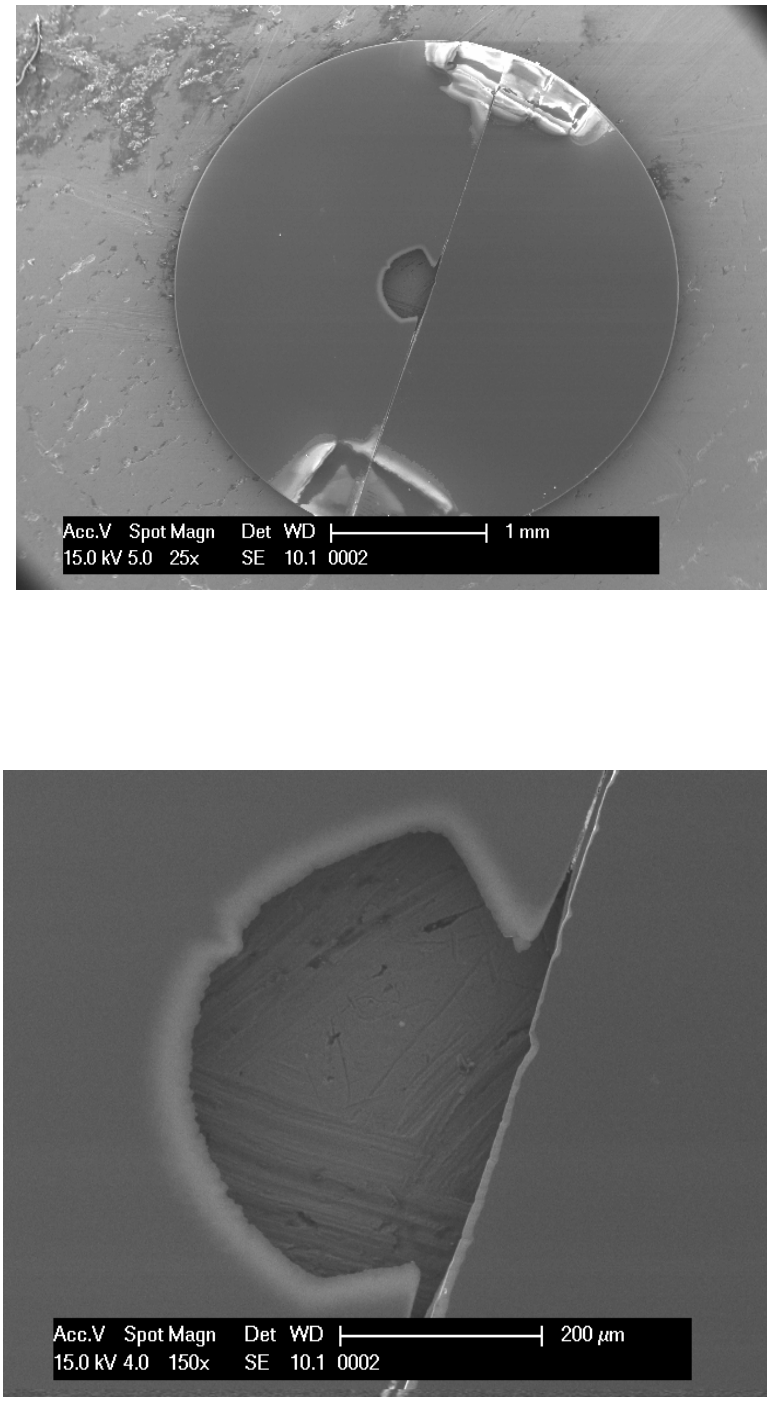


Figure 3.15: Scanning electron microscope (SEM) images of the cross-sectional ion milled diamond TEM sample. TEM investigation were carried out at the edge of the hole at the diamond/diamond interface

Chapter 4

Results

4.1 Layout of the Chapter

This chapter presents results of the initial ion trajectory (TRIM) simulations together with the experimental findings.

4.2 TRIM simulation of ion implantation

Computer simulations of the ion-implantation process were initially done using the TRIM-92 (Transport and Range of Ions in Matter) [10] computer code to simulate the damage distribution produced by the carbon ion multi-implantations, whose parameters were previously given Table 3.1. The Monte Carlo computer code TRIM, statistically follows the trajectories of many ions shot into the target material, by not only calculating the collision history of each ion with the target atoms during the slowing down, but also by accumulating the vacancies and interstitials thus created, yielding, among others, absolute values of the amount and depth profiles of damage caused by ion-implantation to a given dose [58].

Prins [26] observed previously that it is desirable if not essential, in any radiation-damage experiment, to have an average of the defect concentration which, according to Prawer et al. [89] is most applicable for low-temperature

implantations as used in this study, where defect diffusion is minimized.

However, one should bear in mind that although TRIM and similar computer simulations programs give excellent estimates of both the implant and damage profiles, they don't take into account dynamic annealing, recombination or annihilation that occur during interstitial and vacancy migration, or the effect of the gradual accumulation of damage [7, 89, 94].

Figure 4.1 illustrates a typical vacancy distribution as a function of depth. One can see that the average projected range predicted by the Monte Carlo program is $\sim$ 2500Å while the highest level of damage lies at a depth of $\sim$600Å. A displacement energy per atom of 35 eV was used in this simulation. In addition, the mean range of implanted carbon ions with mono-energies between 100 and 300 keV into a carbon host is on the order of 1000-3000 Å [7]. In fact, to be more precise, Djerdj et al. [95] pointed out that while the implantation energy controls the depth profile, the implantation dose and energy determine the local concentration of the implants.

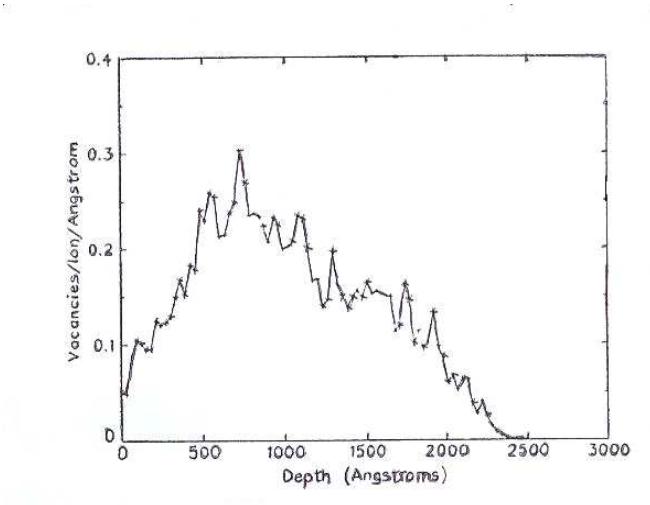


Figure 4.1: A TRIM-92 simulation of the damage (vacancy) distribution produced by the carbon ion multi-implantation. (After ref [10]).

4.3 Bright field transmission electron microscopy and diffraction

All the XTEM specimens were examined using conventional bright field and diffraction imaging techniques in a 200kV Philips CM20 TEM. It is however known that besides providing great information, the electron beam used in TEM may introduce some unwanted radiation damage in the surface or bulk structure of a specimen and thus altering its properties. Fortunately, the thin diamond slices used in this study were imaged safely in the TEM at 200keV accelerating voltage because according to J. Koike et al. [96], the displacement threshold of carbon atoms by incident electrons along the <110> direction only occur above 220keV accelerating voltage.

In bright field mode BF, amplitude contrasted images were obtained by inserting an objective diaphragm in the back focal plane so as to select the transmitted beam only [77]. In addition, for normal imaging, the sample is tilted to a two strong beam condition comprising a directly transmitted beam at the centre of the diffraction pattern plus one other beam for whose planes are at Bragg (the other spots are weak). That is, there is good visibility. The other grains not at this orientation (multiple reflections of similar or varying intensities in the diffraction pattern) will appear considerably less bright or dark.

4.3.1 TEM results of the low dose carbon implanted diamond sample

The TEM micrographs in Figure 4.2 do not show any radiation induced damage in the form of dislocation loops or precipitates. Some threading dislocations propagating from the surface into the ion-damaged diamond and indicated by

D, are visible.

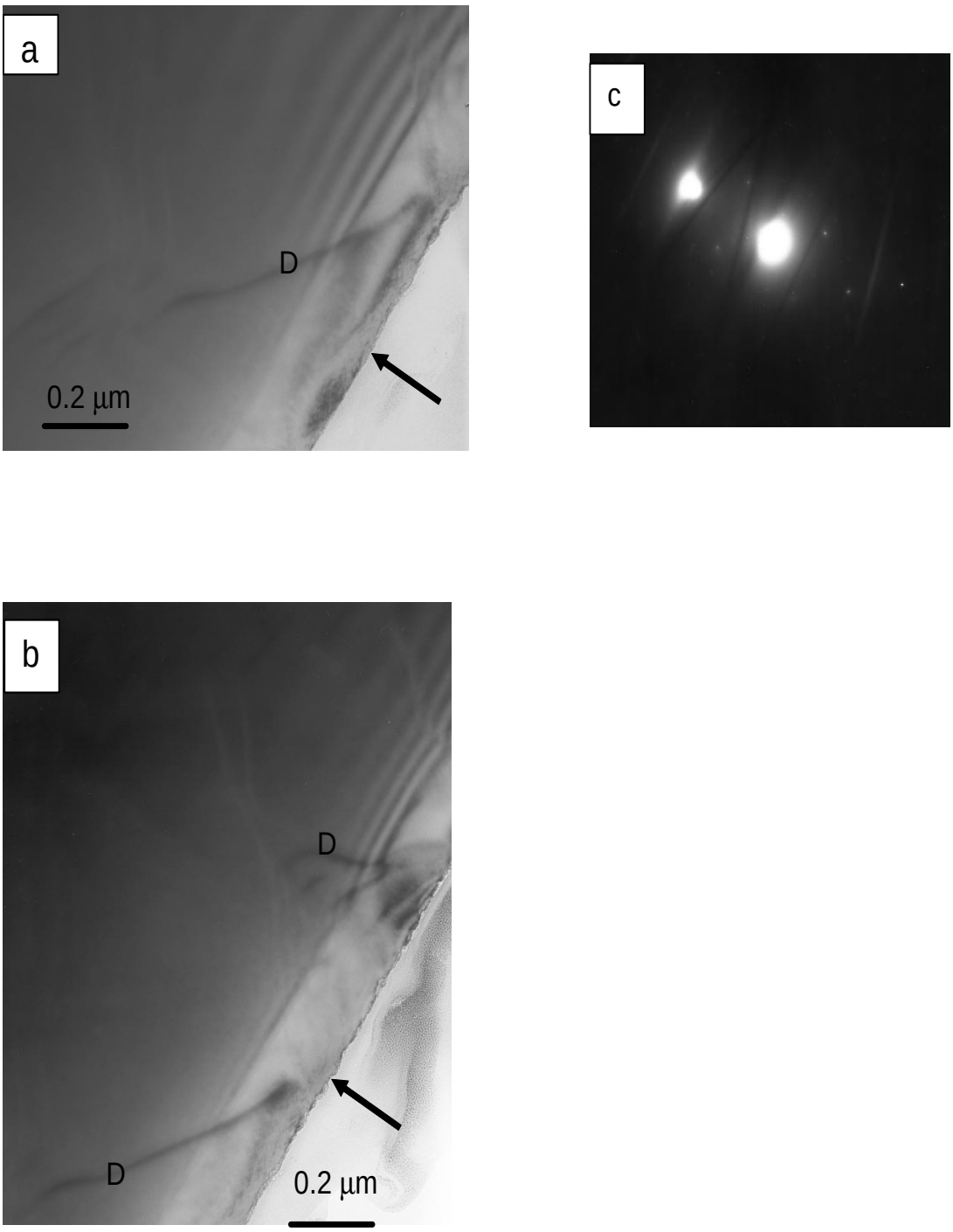


Figure 4.2: Cross-sectional bright-field TEM micrographs and diffraction pattern of the low dose ion-implanted diamond surface . The arrows in (a) and (b) indicate the direction of ion implantation and the point of the arrow shows the diamond/glue interface. The diffraction pattern in (c) indicates that (a) and (b) were recorded with a <110> beam direction and 220 type reflection

.

4.3.2 TEM results of the high dose carbon implanted diamond sample

The TEM micrograph in Figure 4.3 of an unimplanted diamond surface (alongside the arrow) do not show the presence of any dislocations. Indeed, the unimplanted thin diamond was first heated in a vacuum furnace to the braze melting temperature of about 1130K during its mechanical polishing and then annealed to the temperature of 1600K which most likely may have removed all the prominent defects encountered in HPHT-treated single crystal diamonds.

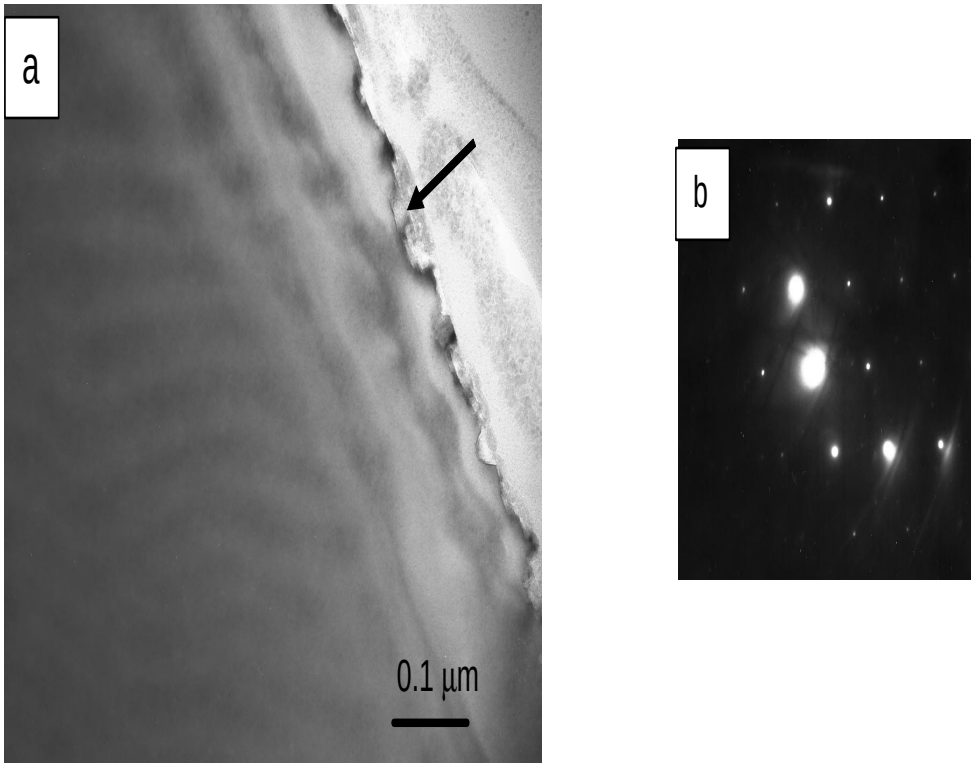


Figure 4.3: Cross-sectional bright-field TEM micrographs and diffraction pattern of an unimplanted diamond surface . The arrow in (a) indicates the diamond/glue interface. The diffraction pattern in (b) indicates that (a) was recorded with a <110> beam direction and 220 type reflection

.

The TEM micrographs in Figure 4.4 all show defect features close to the implanted surface. Since these defects were not present in the unimplanted diamond shown in Figure 4.3, they are most likely the result of ion implantation damage. The dark and bright fringes parallel to the surface in micrographs (a) to (d), are thickness fringes typical of a wedge shaped TEM specimen.

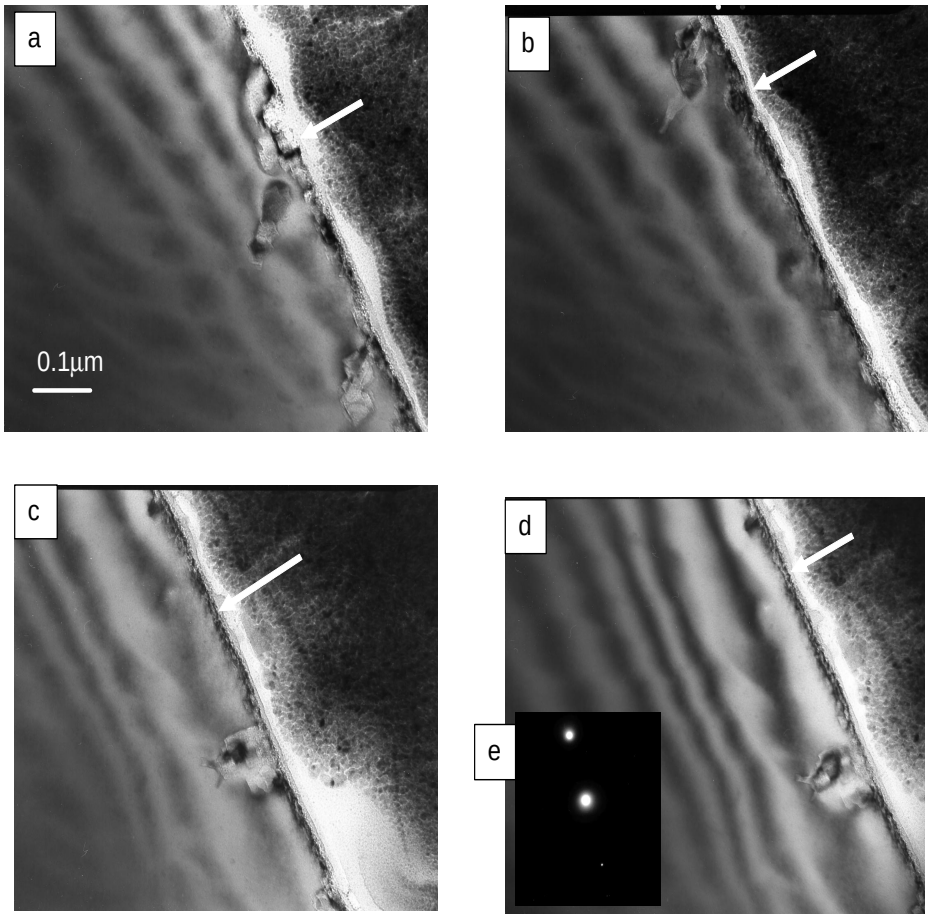


Figure 4.4: Cross-sectional bright-field TEM micrographs and diffraction pattern of the high dose implanted diamond surface . The arrows in (a) to (d) indicate the direction of the ion implantation and the point of the arrow shows the diamond/glue interface. The diffraction pattern in (e) were recorded with a <110> beam direction and 111 type reflection. The magnification of the microcraphs in (a) to (d) are indicated in (a).

.

Chapter 5

Discussion and Conclusions.

5.1 Discussions

At sub-critical implantation doses, it was established that the ion-damaged diamond layer was made essentially of a modest density of threading dislocations, which penetrate deeper (about two times deeper than predicted by TRIM-92) than expected from the interface and running into the bulk of the damaged diamond as shown in Figure 4.2. These findings tally with those obtained by P.F. Lai [4] where they irradiated type IIa diamond with sub-critical doses ($1x10^{13}$ ions/cm^2 and $1x10^{14}$ ions/cm^2) of 320 keV Xe ions at room temperature. Indeed, his transmission electron microscopy (TEM) investigations have revealed dislocations as the predominant native defects in the ion-damaged diamond layer. In addition, Steeds et al. [97] reported observing similar results, i.e., a low density of long straight dislocations normal to the substrate in one of the chemical vapour deposited (CVD) thick single-crystal nitrogen-doped diamond epilayers (c.a. 0.5mm) grown on {001} type Ib substrate which was annealed at high temperature of 1900°C for one hour.

R.A. Spits et al. [98] had already found that annealing of sub-critical implantation doses generates stable defects that lie deeper than 1000Å from the surface in the <100> and <110> channelling directions. They had predicted that those stable defects could be manifestations of dislocations resulting from

the strain generated by the implantation damaged layer.

In addition, annealing of high implantation doses have been shown to introduce deep lying damage into the ion-damaged diamond layer. The penetration of which appears to be temperature dependent; the lower the implant temperature the further the implant damage penetrates [99]. In some cases however, the deep lying damage has been reported to be nearly an order of magnitude, further than the ion range, suggesting that the ^{13}C impinging ions have diffused along and decorated dislocations generated to relieve stresses in the implant zone [6].

A possible explanation of the ultra-deep damage observed in our sub-critical implantation doses results may be due to unavoidable scatter-in (indirect) and direct channelling effects as the beam was oriented perpendicular to the implanted edge along the most open direction [110]. Channelling indeed might not be ruled out because a 7° tilt angle often employed in commercial/research ion implantation equipment while implanting crystalline materials does not prevent it completely [100].

At high implantation doses, the ion-damage consists of some unconventional defect features close to the implanted surface, most likely identified as residual defects on the ion-damaged diamond/virgin diamond interface after unintentionally etching off the 'graphitized' implanted layer during the acid cleaning.

Note in passing that islands of intermediate structure that have been postulated to form for sub-critical doses in the ion-damaged diamond layer [101] haven't been observed in the present study.

5.2 Conclusion

The understanding of radiation damage accompanying ion implantation in diamond is essential for the optimization of p-type and n-type doping as it has been found to be responsible for trapping in doped diamond.

In this work, high-pressure, high-temperature (HPHT) synthetic type Ib diamonds irradiated by carbon ions according to CIRA (cold-implantation-rapid-annealing routine) were investigated using cross sectional transmission electron microscopy namely bright field transmission electron microscopy (BFTEM) coupled with selected area diffraction (SAD).

The analysis of the irradiated HPHT synthetic type Ib diamond at sub-critical implantation doses followed by a rapid thermal annealing (RTA) in a flowing argon atmosphere revealed some line defects identified as threading dislocations propagating deeper than expected, i.e., two times further than the ion range predicted by TRIM-92, from the interface into the bulk of the damaged layer. In contrast to the sub-critical implantation doses, it was found that at very high implantation doses, i.e., above the critical dose, the damaged diamond has got some unconventional defects near the surface which may compromise severely doping applications.

In order to obtain more informative details, further studies may include analyzing the cross-section irradiated specimens using high resolution transmission electron microscopy (HRTEM) coupled with electron energy-loss spectroscopy (EELS) so as to obtain not only high resolution images but also to be able to correlate EELS spectra with defects viewed in HRTEM.

References

[1] S. Prawer, D.N. Jamieson, K.W. Nugent, R. Walker, C. Uzan-Saguy, and R. Kalish, Mat. Res. Soc. Symp. Proc., **647** p. 04.3.1, 2001.

[2] J.F. Prins, Semicond. Sci. Technol., **18** pp. S27–S31, 2003.

[3] M. L. Jenkins and M.A. Kirk, *Characterization of Radiation Damage by Transmission Electron Microscopy.*, IOP Publishing, Oxford, 2001, pp. 2,6.

[4] P.F. Lai, *PhD. Thesis*, University of Melbourne, Australia, 1999, pp. 2,33.

[5] J. C. Vickerman (Edt.), *Surface Analysis: The Principal Techniques.*, John Wiley & Sons, New York, 1997, pp. 6–7.

[6] T.E. Derry, R.A. Spits, and J.P. Sellschop, Mater.Sci.Eng.B, **11** pp. 251,252,255, 1992.

[7] M.S. Dresselhaus and R. Kalish, *Ion Implantation in Diamond, Graphite and Related Materials.*, Springer-Verlag, Berlin, Germany, 1992, pp. 4,5,12,13,30,31,32,37,139,140.

[8] J.O. Orwa, K.W. Nugent, D.N. Jamieson, and S. Prawer, Phys. Rev. B, **62** p. 5462, 2000.

[9] L.W. Yin, Z.D. Zou, M.S. Li, G.L. Geng, D.S. Sun, Z.Y. Hao, and Z.N. Yao, Cryst. Res. Technol., **35,11-12** p. 1289, 2000.

[10] R.A. Spits, J.F. Prins, and T.E. Derry, Nucl. Instr. and Meth. in Phys. Res. B, **85** pp. 347–349, 1994.

[11] R. Kalish, A. Reznik, K.W. Nugent, and S.Prawer, Nucl.Instr. and Meth.B, **148** p. 626, 1999.

[12] A. Tajani, *PhD. Thesis*, Université Joseph Fourier-Grenoble, France, 2003, pp. 26,29.

[13] B.P. Doyle, *PhD. Thesis*, University of the Witwatersrand, 1999, p. 7.

[14] Wikipedia, *Plagiarism...wikipedia; the free encyclopedia*, , 2004. URL `http://en.wikipedia.org/w/index.php?title=Plagiarism &oldid=66316368`. [online; accessed 22-July-2004].

[15] K. Johnston, *PhD. Thesis*, University of London, 2000, p. 22.

[16] B.T. Kelly, *Physics of Graphite*, Applied Science Publishers, London, 1981.

[17] H.O. Pierson, *Handbook of Carbon, Graphite, Diamond and Fullerenes-, Processing and Applications.*, William Andrew Publishing, Noyes, 1993, pp. 44,61.

[18] K. Iakoubovskii, *PhD. Thesis*, Katholieke Universiteit Leuven, 2000, pp. 4,5.

[19] M.N. Latto, *PhD. Thesis*, University of Bristol, 2001.

[20] A. Hoffman, S. Prawer, and R. Kalish, Phys. Rev. B, **45** p. 12736, 1992.

[21] F.P. Bundy, W.A. Basset, M.S. Weathers, R.J. Hemly, H.K. Mao, and A.F. Goncharov, Carbon, **34** pp. 142–143, 1996.

[22] S. Pearce, *PhD. Thesis*, University of Bristol, 2003, p. 3.

[23] *CRC Handbook of Chemistry and Physics, 14^{th} ed.*, CRC Press, NewYork, USA, 1992.

[24] O.W. Palmer, , 2003.04. URL `http://www.semiconductor.co.uk`.

[25] J.B. Wang and G.W. Yang, J. Phys. :Condens. Matter, **11** p. 7090, 1999.

[26] J.F. Prins, Mater. Sci. Rep., **7** pp. 11,278,280,285,291,338, 1992.

[27] G. Davies, J. Phys. C., **9** p. L537, 1976.

[28] J.H.N. Loubser and J.A. van Wyk, *Diamond Conference*, Reading, UK, 1981.

[29] Alexander M. Zaitsev (Edt.), *Optical Properties of Diamond: A Data Handbook.*, Springer-Verlag, Berlin, Germany, 2001.

[30] A.T. Collins. *Course cxxxv.* In Proc. Int. School of Physics, editor, *The Physics of Diamond*, p. 273. IOS PRESS, 1997.

[31] J. Beckman, R.B. Jackman, and J.S. Foord, Diam. & Relat. Mater., **3** p. 602, 1994.

[32] G.S. Woods, I. Kiflawi, W. Luyten, and G. van Tendello, Phil. Mag. Letters, **67** p. 405, 1993.

[33] K. Haenen, *PhD. Thesis*, Universeit Limburg, 2002, p. 8.

[34] I.Z. Machi, *MSc. Thesis*, University of Durban-Westville, 1996, p. 6.

[35] A.T. Collins, Physica B., **185** p. 284, 1993.

[36] R.F. Davis, *Handbook on Semiconductors,Ed. T.S. Moss.*, Elsevier Science, Amsterdam, 1994.

[37] H. Liu and D.S. Dandy, *Diamond Chemical Vapor Deposition: Nucleation and Early Growth Stages.*, Noyes Publications, Park Ridge, 1995.

[38] R. Pereira, *PhD. Thesis*, University of Aveiro, 2002, p. 7.

[39] R.C. Burns and G.J. Davies. In J.E. Field, editor, *The Properties of Natural and Synthetic Diamond*. Academic Press, London, 1993.

[40] A.T. Collins, H. Kanda, J. Isoya, C.A.J. Ammerlaan, and J.A. van Wyk, Diam. & Relat. Mater., **7** p. 33, 1998.

[41] R.C. Burns, J.O. Hansens, R.A. Spits, M. Sibanda, C.M. Welbourn, and D.L. Welsh, Diam. & Relat. Mater., **8** pp. 1433–1434, 1999.

[42] P.W. May, Endeavour Mag., **19** p. 101, 1995.

[43] S. Shikata, MRS Bulletin, **23** p. 61, 1998.

[44] J.T. Glass, B.A. Fox, D.L. Dreisfus, and B.R. Stoner, MRS Bulletin, **23** p. 49, 1998.

[45] C. Picirolli, G. Davies, A. Mainwood, and C.M. Penchina, Diam. & Relat. Mater., **11** pp. 338–341, 2002.

[46] A.T. Collins and A.W.S. Williams, J. Phys. C, **4** p. 1, 1971.

[47] R.J. Farrer, Solid State Commm., **7** p. 685, 1969.

[48] J.F. Prins, Nucl. Instr. and Meth. in Phys. Res. A, **514** pp. 69–70, 2003.

[49] V.S. Vavilov, Radiat. Eff. Defect. S., **37/3-4** p. 229, 1978.

[50] S. Koizumi, H. Ozaki, M. Kamo, Y. Sato, and T. Inuzuka, Appl. Phys. Lett., **71** p. 1065, 1997.

[51] S. Koizumi, M. Kamo, S. Mita, A. Sawabe, A. Reznik, C. Uzan-Saguy, B. Rau, and R. Kalish, Diam. & Relat. Mater., **7** p. 540, 1998.

[52] J.F. Prins, Semicond. Sci. Technol., **16** p. L50, 2001.

[53] W.K. Chu, J.W. Mayer, and M.A. Nicolet, *Backscattering Spectroscopy.*, Academic, Newyork, 1978.

[54] L.C. Feldman, J.W. Mayer, and S. Picraux, *Materials Analysis by Ion Channelling.*, Academic, Newyork, 1982.

[55] R. Kalish, Diam. & Relat. Mater., **2** p. 622, 1993.

[56] J. Ziegler, J.P. Biersack, and U. Littmark, *In the Stopping Range of Ions in Solids.*, Pergamon, Newyork, 1982.

[57] . URL `http://www.mse.vt.edu.faculty/hendricks/mse4206/GaAsTEK/ionimplant/advanced.htm`.

[58] R. Kalish, A. Reznik, A. Prawer, D. Saada, and J. Adler, phys. stat. sol. (a), **174** pp. 83,84,93, 1999.

[59] P. D. Townsend, J.C Kelly, and N.E.W. Hartley, *Ion Implantation , Sputtering and their Applications.*, Academic Press, Newyork, 1976, pp. 65,68,84,85.

[60] J.N. Spencer, G.M. Bodner, and R.H. Richard, *Introduction to solid state chemistry:the imperfect solid state*, , 2002. URL `http://web.mit.edu/3.091/www/archives/Notes_6.pdf`.

[61] S.J. Breuer and P.R. Briddon, Phys. Rev. B., **51** p. 6984, 1995.

[62] D. Saada, J. Adler, and R. Kalish, Int. J. Mod. Phys. C, **9,No.1**, 1998.

[63] D. Saada, *PhD. Thesis*, Israel Institute of Technology, 2000.

[64] . URL `http://www.answers.com`.

[65] A.T. Blumenau, *PhD. Thesis*, der Universität Paderborn, 2002, pp. 18,19,21,22,120.

[66] C. Kittel, *Introduction to solid State Physics, 7^{th} ed.*, Wiley & Sons, Inc, Newyork, 1996, pp. 588–595.

[67] D. R. Askeland, *The Science and the Engineering of Material, S.I Adaptation by F. Haddleton, P. Green, H. Roberston.*, Chapman & Hall, 2-6 Boundary Row, London, 1996, pp. 97–101.

[68] J.P. Hirth and J. Lothe, *Theory of Dislocations,2nd ed.*, Wiley, New York, 1982.

[69] P. Humble and R.H.J. Hannink, *Nature, 273*, London, 1978, p. 37.

[70] N. Sumida and A.R. Lang, *Cathodoluminescence and TEM studies of Dislocation-Rich Natural Diamonds, in Microscopy of Semiconducting materials,edited by A.G. Cullis and D.C. Joy (Institut of Physics, Bristol), no.60 in conference series.*, London, 1981, p. 319.

[71] P. Pirouz, D.J.H. Sumida, Sir P. Hirsh, and A.R. Lang, Appl. Phys. Lett., **60** p. 3138, 1983.

[72] J. C. Anderson, K.D. Leaver, R.D. Rawlings, and J.M. Alexander, *Materials Science, 4^{th} ed*, Chapman & Hall, UK, 1995, pp. 156–174.

[73] R.F. Ergeton. *Private Communication.*

[74] *Instruction manual production Ion Implanter model 200-20AF*, Chapman & Hall, Blackburn Industrial Park, Gloucester, 1977.

[75] . URL `www.namotec.com/images/TL/Improving High Resolution TEM images using Low energy Ion Mi.pdf`.

[76] . URL `http://micron.ucr.edu/public/gatan/pips-691.html.`

[77] C. Cayron, *PhD. Thesis*, Ecole Polytechnique Fédérale de Lausanne, 2000, pp. 21,34,32,35.

[78] Z.L. Wang, J. Phys. Chem. B., **104** pp. 1155–1156, 2000.

[79] P.B. Hirsh, A. Howie, R.B. Nicholson, D.W. Pashley, and M.J. Whelan. *J. electron microscopy of thin crystals.* Roberts E. Krieger Publishing Company, New York, 1977.

[80] R.F. Ergeton, Microsc. Microanal. (Suppl2), **9** pp. 1562–1563, 2003.

[81] *Introduction of transmission electron microscopy (tem) and sample preparation*, . URL `http://nstg.nevada.edu/TEM/unlv.`

[82] S. Horiuchi and L. He. *High-resolution transmission microscopy.* In N.D. Browning and S.J. Pennycook, editors, *Characterization of High Tc Materials and Devices by Electron Microscopy*, p. 53. Cambridge University Press, London, 2000.

[83] M. Rebak, J.P.F. Sellschop, and S.H. Connel, Nucl. Instr. & Meth. B, **85** p. 246, 1994.

[84] F. M. van Bouwelen, Diam. & Relat. Mater., **9** p. 925, 2000.

[85] S.E.Grillo, J.E.Field, and F.M van Bouwelen, J.Phys. D:Appl. Phys., **33** pp. 985–990, 2000.

[86] M.R. Jarvis, R. Pérez, F.M van Bouwelen, and M.C. Payne, Phys. Rev. Lett., **80** p. 3431, 1998.

[87] R.A. Spits, J.F. Prins, J.D. Comins, and T.E. Derry, S. Afr. J. Phys., **16 No.1/2** p. 17, 1993.

[88] J.F. Prins, Phys. Rev. B, **38** p. 5579, 1988.

[89] S. Prawer and R. Kalish., Phys. Rev. B, **51** pp. 15712,15714,15715, 1995.

[90] S. Prawer, Diam. & Relat. Mater., **4** p. 864, 1995.

[91] . URL `http://www.dynalabcorp.com/catalog_ STC.asp`.

[92] J.F. Prins, Diam. & Relat. Mater., **8** pp. 1635–1637, 1999.

[93] Á. Barna, B. Pécz, and M. Menyhárd, Micron, **30** pp. 267–276, 1999.

[94] C. Saguy, A. Reznik, Z. Remes, and R. Kalish, Diam. & Relat. Mater., **13** p. 723, 2004.

[95] I. Djerdj, A.M. Tonejc, M. Bijelić, M. Buljan, U.V. Desnica, and R. Kalish. *Private Communication.* 2005.

[96] J. Koike, D.M. Parkin, and T.E. Mitchell, Appl. Phys. Lett., **60** p. 1450, 1992.

[97] J.W. Steeds, A.E. Mora, H.M.B. Darwis, J.M. Hayes, J.E. Butler, and D. Fisher, *The 55th Diamond Conference*, Warwick, UK, 2004.

[98] R.A. Spits, T.E. Derry, and J.F. Prins, Nucl. Instr. and Meth. in Phys. Res. B., **64** p. 212, 1992.

[99] R. A. Spits, W. Baloyi, and T. E. Derry, Phys. Rev. C., **41 No. 5** pp. 2429–2431, 1990.

[100] R. Simonton and A.F. Tasch. *Channelling effects in ion implantation.* In J.F. Ziegler, editor, *Handbook of Ion Implantation Technology*, p. 21. Elsevier Science Publisher B.V, North-Holland, 1992.

[101] R.A. Spits, *PhD. Thesis*, University of the Witwatersrand, 1993, p. 161.